Sapphirine-bearing pyroxenite xenoliths in Cenozoic alkali basalt from Jabel El Arab (Syria): insights into the nature and composition of the lithosphere beneath the southern Syrian Rift, northern part of the Arabian Plate

Mohamed Ismail, Guillaume Delpech, Bertrand N. Moine, Michel Grégoire, Colette Guilbaud, Jean-Yves Cottin

Journal Pre-proofs

Sapphirine-bearing pyroxenite xenoliths in Cenozoic alkali basalt from Jabel El Arab (Syria): insights into the nature and composition of the lithosphere beneath the southern Syrian Rift, northern part of the Arabian Plate

Mohamed Ismail, Guillaume Delpech, Bertrand Moine, Michel Grégoire, Colette Guilbaud, Jean-Yves Cottin

PII: S1367-9120(19)30498-5
DOI: https://doi.org/10.1016/j.jseaes.2019.104146
Reference: JAES 104146

To appear in: *Journal of Asian Earth Sciences*

Received Date: 6 September 2019
Revised Date: 11 November 2019
Accepted Date: 12 November 2019

Please cite this article as: Ismail, M., Delpech, G., Moine, B., Grégoire, M., Guilbaud, C., Cottin, J-Y., Sapphirine-bearing pyroxenite xenoliths in Cenozoic alkali basalt from Jabel El Arab (Syria): insights into the nature and composition of the lithosphere beneath the southern Syrian Rift, northern part of the Arabian Plate, *Journal of Asian Earth Sciences* (2019), doi: https://doi.org/10.1016/j.jseaes.2019.104146

Sapphirine-bearing pyroxenite xenoliths in Cenozoic alkali basalt from Jabel El Arab (Syria): insights into the nature and composition of the lithosphere beneath the southern Syrian Rift, northern part of the Arabian Plate

Mohamed Ismail[1], Guillaume Delpech[2], Bertrand Moine[3], Michel Grégoire[4], Colette Guilbaud[3], and Jean-Yves Cottin[3]

[1]Department of Geology, University of Aleppo, Aleppo, Syria. email: ismail_975@yahoo.fr

[2]GEOPS, Université Paris-Sud, CNRS, Université Paris-Saclay, Rue du Belvédère, Bât. 504-509, 91405 Orsay, France, guillaume.delpech@u-psud.fr

[3]Université Lyon, UMR-CNRS-UCA-UJM-IRD 6524, 23 rue du Dr P. Michelon, 42023 Saint-Étienne, France, bertrand.moine@univ-st-etienne.fr; colette.alboussiere@univ-st-etienne.fr; jean.yves.cottin@univ-st-etienne.fr

[4]Geosciences Environnement Toulouse, UMR5563-CNRS-CNES-IRD-UPS, Observatoire Midi-Pyrénées, 14 Av. E. Belin, 31400 Toulouse, France, michel.gregoire@get.omp.eu

Corresponding author: Jean-Yves Cottin, Univ.Lyon, UMR-CNRS-UCA-UJM-IRD 6524, 23 rue du Dr P. Michelon, 42023 Saint-Étienne, France. jean.yves.cottin@univ-st-etienne.fr

Abstract

Pyroxenites and composite xenoliths occur in the Cenozoic alkali basalts of Jabel El Arab (the southern extremity of the Syrian Rift). The anhydrous xenolith suite consists mainly of spinel garnet-sapphirine–bearing websterites, spinel-olivine–bearing websterite, as well as rare spinel plagioclase-garnet–bearing websterites and composite garnet-bearing websterite/anorthosite xenoliths. We report for the first time sapphirine coronas around spinel in spinel-garnet–bearing websterite xenoliths from two outcrops in this region. Their compositional and microstructural features are consistent with a reaction from spinel + orthopyroxene + anorthite to clinopyroxene + garnet + sapphirine. The full pyroxenite suite is divided into two groups based on mineralogical characteristics and geochemical composition: (A) tholeiitic to transitional mantle segregates having spinel ± garnet ± sapphirine characterized by a high Al_2O_3 and CaO content, low REE content, LREE depletion, and a highly variable Sr-Nd isotopic ratio; (B) alkaline segregates that include spinel-olivine–bearing websterite and composite xenoliths characterized by a high TiO_2 and alkali content, relatively high REE, and low Ni and Cr. Slight LREE enrichments in clinopyroxenes from meta-igneous rocks of tholeiitic to alkaline affinity indicate that they were later metasomatized by small volumes of percolating silicate melts in the upper lithospheric mantle. The xenoliths have been re-equilibrated within the garnet-pyroxenite stability field. Combining xenolith-derived P-T estimates with mineral and chemical composition and seismic data, we show that the websterite xenoliths formed in the shallow lithospheric mantle near the Moho discontinuity at 28–44 km in depth. Nd-model ages and the geodynamic history of the Arabian Plate favor the scenario of tholeiitic-transitional and alkaline magmas being underplated below or intruded at the base of a thinned Syrian crust. This occurred around 200–100 Ma in response to rifting and magmatism beneath the Arabian Plate during the early assembly of the eastern Mediterranean region.

Keywords: Syrian Rift, pyroxenite xenoliths, upper mantle, sapphirine, tholeiitic/alkaline affinity, Jabel El Arab

Highlights

- Spinel-garnet-sapphirine-websterite xenoliths have a tholeiitic affinity.
- Spinel-olivine-plagioclase-websterites have an alkaline affinity.
- Composition of clinopyroxenes is consistent with metasomatism by silicate melts.
- Websterite xenoliths originated from the shallow lithospheric mantle.
- Websterite xenoliths highlight crustal growth of the eastern Mediterranean Province.

1. Introduction

Cenozoic alkaline volcanic rocks of the Harat Ash Shamm contain a large variety of ultramafic and mafic xenoliths derived from the crust and upper mantle. Previous studies of crustal granulites and mantle-derived ultramafic xenoliths from the northern part of the Arabian Plate, particularly beneath the Dead Sea fault system (DSFS), focused mostly on petrographical and geochemical descriptions of mantle xenoliths and their Neogene–Quaternary host basalts (McGuire and Stern 1993; Medaris and Syada 1998; Nasir and Safarjalani 2000; Bilal and Touret 2001; Bilal and Sheleh 2004; Al-Mishwat and Nasir 2004; Al-Fugha and Al-Amaireh 2007; Shaw et al. 2007; Ismail et al. 2008; Ismail 2008; Nasir and Rollinson 2008; Al-Safarjalani et al. 2009, Krienitz and Haase. 2010, Stern and Johnson. 2010, Trifono et al. 2011, Asfahan, 2011, Malpas et al., 2011; Nasir and Stern, 2012).

Unlike mantle peridotitic xenoliths the composition of Syrian lithospheric deep segregates remain poorly documented, especially with regard to the links between modal mineral and isotopic compositions and their relationships to both rheological data at the Moho and tectonic history. Websterite, orthopyroxenite, and clinopyroxenite represent likely <5% of the upper mantle (Fabriès et al., 1991; Hirschman and

Stopler, 1996). The study of pyroxenite xenoliths carried by Neogene–Quaternary basalts from southern Syria provides a great deal of information regarding the composition and evolution of the mantle beneath a thinned continental lithosphere. Although mantle xenoliths have been studied in the Arabian Plate region, their origin and evolution have been much less considered.

This paper reports new petrographical, mineralogical, and geochemical data for a suite of pyroxenite xenoliths originating from Jabel El Arab volcanism in southern Syria (Harat Ash Shamm: Tel Tannoun, Tel Imtan El Koudre, and Tel El Ajailate). The investigated xenolith suite comprises spinel-websterites and composite websterite/anorthosite xenoliths. Sapphirine coronas are described around spinel associated with or without garnet coronas in the websterite xenoliths (Ismail, 2008). This study aims to assess the nature and origin of these websterite xenoliths via whole-rock analyses and in situ trace element analyses of clinopyroxenes by LA-ICP-MS combined with new isotopic data on clinopyroxenes. The geochemical affinity and the clinopyroxene isotopic compositions of the websterite xenoliths are discussed in relation to the geodynamic context of the Arabian Plate and the magmatic evolution and crustal growth of the eastern Mediterranean provinces. Geochemical and seismic data are then combined to construct a model of the dynamics of the lower crust and upper mantle beneath the southern Syrian Rift since the late Proterozoic.

2. Geological setting and xenolith occurrence

Present-day Syria is situated in the northwestern portion of the Arabian Plate, and its western edge represents the northern Levantine continental margin. The Syrian Rift extends northwards for approximately 1000 km from the Dead Sea fault system and forms the boundary between the African and Arabian plates. Volcanism along the Syrian Rift is related to the movement of the Arabian Plate toward the Eurasian Plate at a velocity of 18 ± 2 mm/year in a north–northwesterly direction (McClusky et al. 2000; Fig. 1). Previous studies indicate that the lithosphere of the Arabian Plate formed through

Neoproterozoic accretion of island arcs and microplates against northeast Africa, ca. 950–640 Ma, as part of the widespread pan-African orogeny (Beydoun 1991; Brew et al. 2001a, Stern and Johnson, 2010). This was followed by continental rifting and intercontinental extension between 620 and 530 Ma (Husseini 1989). The study region then became part of the northern passive margin of Gondwana for most of the Phanerozoic (Brew et al., 2001a; Adiyaman and Chorowicz, 2002). Seismic data indicates that the metamorphic Precambrian basement in Syria varies between 6 and 8 km in depth (McBride et al., 1990; Brew et al., 2001b). The thickness of the platform deposits reaches 10-km thick in the eastern part of the Arabian Plate. These platform deposits consist mainly of Phanerozoic sediments. Volcanism in Syria can be divided into two distinct periods: Upper Jurassic–Lower Cretaceous (Dubertret, 1933), and Neogene–Quaternary (Mouty et al., 1992; Nasir and Safarjalani, 2000). Neogene–Quaternary alkali-basalt volcanism relates to the formation of the Red Sea (24–16 Ma) and Dead Sea rifts 8–0.4 Ma (Bohannon et al., 1989; Camp and Roobol, 1989; Nasir, 1994; Baker et al., 1997; Chorowicz et al., 2005). The Syrian Rift therefore represents the northern portion of the Dead Sea Rift and is the continuation of the Red Sea Rift. Neogene basalts from southern Syria are mostly alkali basalts and basanites (Stein and Hofmann, 1992; Stein et al., 1993; Laws and Wilson, 1997, Ismail, 2008, Ismail et al., 2008). Geochemical studies of volcanic rocks from the southern Arabian Plate (Yemen and Jordan) indicate that the interaction between the rising Afar asthenospheric mantle plume and the lithospheric mantle generated this volcanism (Camp and Roobol, 1989; Nasir, 1994, Baker et al., 1997). More recent geochemical studies of lavas from the northern portion of the Arabian Plate (Harat Ash Sham; Syria, Jordan) favor, rather, an origin of the volcanism due to asthenospheric upwelling in response to lithospheric extension in this region and do not assign any role for the Afar mantle plume (Shaw et al., 2003; Lustrino and Sharkov, 2006; Weinstein et al., 2006). Nonetheless, recent isotopic data of mantle xenoliths entrained in late Cenozoic lavas from northwest Jordan suggest that the Arabian lithospheric mantle protolith formed from an already depleted mantle source that first formed during the accretion

and growth of the pan-African crust, ca. 700 Ma (Shaw et al., 2003, 2007). The long-term evolution of this portion of lithospheric mantle could represent a source region for Arabian intraplate volcanism. The study area of Jabel El Arab represents the northwestern boundary of the Arabian Plate (Fig. 1). Most of the Cenozoic volcanic fields in Syria are located along secondary faults with a N–S direction parallel to the Syrian Rift. The most widespread occurrence of alkali lavas (Neogene–Quaternary) is concentrated in southern Syria, as a linear zone parallel to the principal direction of the Syrian Rift. The Cenozoic basaltic lavas may be up to 1500-m thick and are covered by Tertiary and Quaternary sediments (Nasir and Safarjalani, 2000; Al-Mishwat and Nasir, 2004). We sampled xenoliths collected from the Neogene–Quaternary volcanic field of Jabel El Arab (belonging to Harat Ash Shamm), south of Damascus, from Tel Tannoun (latitude: 32°57′, longitude: 36°44′), Tel Imtan El Koudre, located near the Jordanian border with Syria (latitude: 32°25′, longitude: 36°48′), and Tel El Ajailate (latitude: 32°46′, longitude: 36°47′) (Fig.1). These xenoliths occur around the flanks and within craters of strombolian volcanic cones. Most of these websterite xenoliths are rounded to subrounded in shape. They range in size from a few centimeters to more than 20 cm in diameter.

3. Analytical methods

We determined modal compositions by point counting (3000 points per thin section). We selected 18 websterite xenoliths for mineralogical and geochemical analyses; major element compositions of bulk rock powders were then determined by X-ray fluorescence spectrometry (XRF) at the École des Mines de St-Étienne (France). Typical detection limits ranged from 0.01 to 0.06 wt% for CaO, Cr_2O_3, Fe_2O_{3total}, K_2O, MgO, MnO, Na_2O, P_2O_5, and TiO_2. Detection limits were 0.20 and 0.50 wt% for Al_2O_3 and SiO_2, respectively. We determined the concentrations of rare earth elements (REE) using inductively coupled plasma mass spectrometry (ICP-MS) at the Observatoire Midi-Pyrénées (University Paul Sabatier, Toulouse, France). For our analyses, 100 mg of powdered sample was dissolved in concentrated

HF/HNO_3 within closed Savillex Teflon beakers. Following digestion, samples were evaporated to incipient dryness, dissolved in concentrated 2M-HNO_3, and again evaporated to incipient dryness. We then transferred the sample solutions into 50-mL centrifuge tubes, and we filled the tubes to 50 mL using internal standard stock solutions. For ICP-MS, solution/sample ratios were >1000–1200. We also ran several reference materials (UB-N, JP-1, BE-N) on the ICP-MS with each sample batch to verify accuracy and precision. Detection limits were 1–5 ppb for most REE and 5–30 ppb for Ce and Sm. Average within-run precision (%RSD) was better than 5% for Er, Tm, Yb, and Lu, and better than 3% for all other REE.

We also measured Sr and Nd isotopic ratios for five fresh clinopyroxenes (~150 mg) using a Finnigan MAT261 mass spectrometer at the Observatoire Midi-Pyrénées (University Paul Sabatier, Toulouse, France). Sr and Nd were collected using Sr-Spec, TRU-Spec, and LN-Spec resins. We verified the accuracy of the measurements using the NIST SRM 987 geostandard for $^{87}Sr/^{86}Sr$ (0.710271 ± 9) and the La Jolla geostandard for $^{143}Nd/^{144}Nd$ (0.511839 ± 6).

Electron microprobe analyses of minerals were obtained using a CAMECA SX-100 (CNRS-UMR 6524, Clermont-Ferrand, France) with wavelength-dispersive spectrometry (WDS). Operating conditions were 15 kV accelerating voltage, 15 nA beam current for mineral analyses with a beam diameter of ~2–3 μm. We used natural and synthetic minerals as standards. For all elements, counting times were 10 s for peaks and 10 s for background. Detection limits were typically 0.01–0.04 wt%. We also measured the concentrations of 27 elements (REE, Ba, Rb, Th, U, Nb, Pb, Sr, Zr, Hf, Ti, Y, Sc, V, and Ni) in clinopyroxenes from 120-μm thick polished sections using an LA-ICP-MS at the Observatoire Midi-Pyrénées (University Paul Sabatier, Toulouse, France). This system comprises a CETAC LSX-200 frequency-quadrupled Nd-YAG laser ablation system that delivers a wavelength of 266 nm connected to a Perkin Elmer Elan 6000 ICP-MS (Grégoire et al., 2002). A typical analysis consists of three replicates

of 100 readings; each replicate represents one sweep of the mass range. The counting time for one sample was typically 160–170 seconds. We used the NIST 610 and 612 glass standards as external standards, and normalized the analyses using the Ca wt% values determined by electron microprobe. The ablated material was carried from the laser cell to the ICP-MS using a mixture of He and Ar. Typical detection limits ranged from 10–20 ppb for REE, Ba, Rb, Th, U, Nb, Ta, Sr, Zr, Hf, and Y, 100 ppb for V and Sc, and 2 ppm for Ti, Ni, and Cr. The typical precision and accuracy for LA-ICP-MS analyses ranged from 1% to 10%.

4. Petrography

All studied pyroxenite xenoliths are websterites (17 samples) and one composite websterite/anorthosite (IT41) (Table 1). They contain variable amounts of spinel (0.5–18.5 vol%), except for the composite xenolith IT41. Only one sample displays plagioclase (ca. 1 vol% in IT26). We distinguished two groups based on mineralogical characteristics (shown in Table 1). Group (A) is composed of spinel ± garnet ± sapphirine xenoliths, and Group (B) is composed of spinel ± olivine ± plagioclase xenoliths. Microstructures in xenoliths are usually coarse-grained and locally coarse grain-tabular to rare porphyroclastic, based on the classification of Mercier and Nicolas (1975). Clinopyroxene and orthopyroxene vary in size from 1 to 10 mm, and they usually show rectilinear grain boundaries. Both pyroxene porphyroclasts are commonly deformed. They display spongy rims in some spinel±garnet±sapphirine–bearing websterites (Group A: 12Th, 15Th, 16Th, and 20Th). Large pyroxene grains containing abundant exsolution lamellae of spinel and garnet are a common characteristic in most studied Syrian websterites (Fig. 2). Spinel occurs both as xenomorphic or subautomorphic crystals and as exsolution lamellae in most pyroxene porphyroclasts. Spinel is green in most samples and brownish in websterites containing olivine (Group B: II10, II31, and IT23). Their grain size ranges from 0.3 to 1 mm, although larger grains reach up to 15 mm. Small crystals of orthopyroxene and rare clinopyroxene

are enclosed within large spinels of websterite IT28 (Group A) (Fig. 2a). Three spinel-garnet–bearing websterites (Group A: IT2, IT28, and 15Th) show significant replacement of thin garnet corona by spinel (Fig. 2e and f). We observed spongy rims of spinel only in the websterite sample 16Th (Group A). The proportion of garnet varies (2–10 vol%) in most websterites and appears commonly in the form of coronas around spinel or sapphirine (Fig. 2a, b, c) as xenomorphic crystals (0.2–2 mm) or exsolution lamellae. Some websterites show replacement of thin garnet coronas by kelyphite, similar to that described by Grégoire et al. (1994, 1998, 2001) for oceanic garnet granulite xenoliths from the Kerguelen Archipelago. Although several petrological and geochemical studies have examined cumulate xenoliths within the large volcanic massif of Jabel El Arab (Sharkov et al., 1993; Nasir and Safarjalani, 2000; Al-Mishwat and Nasir, 2004; Bilal and Touret, 2001), only Ismail (2008) reported sapphirine-bearing meta-igneous rocks in pyroxenite xenolith suites from the Syrian region. Our observation of sapphirine therefore constitutes an original petrological feature of the base of the crust or upper mantle beneath the Syrian Rift. We observed sapphirine in some websterite xenoliths (Table 1) from Tel Tannoun and Tel El Ajailate. This sapphirine has colorless or slightly blueish grains under polarized light and always surrounds spinel with or without garnet having coronas of millimetric thickness (Fig. 2c). Microstructural relationships between the three aluminous phases (spinel-garnet-sapphirine) in the studied websterites suggest two reactions at high pressure and temperature: (1) clinopyroxene+orthopyroxene+spinel to garnet, and (2) spinel+orthopyroxene+anorthite to clinopyroxene+garnet+sapphirine. Reaction (1) explains the formation of garnet, whereas reaction (2) indicates the formation of sapphirine and garnet coronas (Fig. 2a, b, c). Olivine characterizes, in particular, the two samples from Tel Imtan El Koudre (II10 and II31) and one xenolith (IT23) from Tel Tannoun which shows undulose extinction. Olivine is slightly altered and ranges in size from 0.5 to 3 mm. Orange-colored pargasite displays coronal textures around clinopyroxene in websterite IT26 and the composite xenolith IT41. We also observed pargasite as exsolution lamellae in pyroxene porphyroclasts of the websterite IT26. In the composite xenolith IT41,

a plagioclase-rich area is cross-cut by veins of clinopyroxenite (Fig. 2d) and, locally, orthopyroxenite. Porphyroclasts of plagioclase (1–5 mm) are more abundant at the contact with the pyroxenite (Fig. 2d). This composite xenolith is also extremely rich in titanomagnetite; titanomagnetite occurs in the coronas surrounding garnet as small grains enclosed in clinopyroxene porphyroclasts or as large subautomorphic crystals (ca. 8 mm) (Fig. 2d). Magnetite associated with titanomagnetite occurs in some samples (IT23, IT26, IT28, IT45, and IT53) in both groups as secondary minerals. The websteritic part of the composite xenolith IT41 (Group B) displays petrographical and microstructural characteristics similar to the other websterites. Garnet exsolutions in orthopyroxene grains in the spinel-amphibole-garnet-plagioclase–bearing websterite (Fig. 2e) is a characteristic feature of IT26 (Group B). Orthopyroxene porphyroclasts locally enclose small garnet crystals (Fig. 2f) in the spinel-garnet–bearing websterite IT8 (Group A). Clinopyroxene and orthopyroxene porphyroclasts of the xenolith suite frequently contain variable amounts of solid inclusions and fluid inclusions of CO_2, similar to those described in mantle xenoliths from Tel Tannoun by Bilal and Touret (2001); however, these inclusions are more abundant and larger than those observed in other Syrian mantle xenoliths, defined as Type I. The Syrian websterites can be classified according to the presence or absence of specific minerals, including garnet, olivine, sapphirine, and plagioclase (Table 1).

5. Mineral major element composition

5.1. Olivine

Olivine only occurs in Group B websterite xenoliths (samples II10, II31, and IT23) and is commonly very magnesian. The Mg# = [Mg/(Mg+Fe^{2+})] × 100) in the websterites of Tel Imtan El Koudre site (94.4–96.6) is clearly higher than that of the xenolith from Tel Tannoun (81.4–84.4). At Tel Imtan El Koudre (Group B), olivine could originate from mantle peridotites to explain such a disequilibrium. The NiO

content of olivines is relatively homogeneous (0.17–0.32 wt%). Concentrations of CaO are always <0.11 wt%.

5.2. Orthopyroxene

All analyzed orthopyroxenes have enstatite compositions that range from En68.3 to En91.8. The Mg# is commonly homogeneous within each group and shows a slight decrease from Group A (81–90) to Group B xenoliths (69.6–89.2). These orthopyroxenes are characterized by Al_2O_3 >2.3 wt%. Higher concentrations of Al_2O_3 occur in orthopyroxene of Group A websterites (4.77–8.17 wt%) relative to the concentrations in the orthopyroxene of Group B websterites (2.3–6.65 wt%). The Cr_2O_3 content is usually low (<0.68 wt%). A positive correlation between Al_2O_3 and both Cr_2O_3 and Mg# is observed in orthopyroxene.

5.3. Clinopyroxene

Clinopyroxenes are commonly aluminous diopsides ($3.24 < Al_2O_3 < 9.22$ wt%), except for one spinel-olivine–bearing websterite (Group B: IT23) and two clinopyroxenes from spinel-amphibole-garnet-plagioclase–bearing websterites (Group B: IT26) that show an Al-augite composition. The Mg# decreases progressively from Group A websterites (83.06–91.7) to Group B websterites (70.78-88.4) to the composite websterite/anorthosite (68.9–70.8) (Fig. 3). The CaO content of clinopyroxenes is usually homogeneous in Group A (21.1–23.26 wt%), while highly variable in Group B websterites (17.35–23.27 wt%). The highest Cr_2O_3 concentrations characterize the spinel-garnet-sapphirine websterites (0.07–0.96 wt%), whereas the composite sample IT41 (Group B) displays the lowest concentration (< 0.06 wt%). The clinopyroxenes of Group B websterites are characterized by a higher TiO_2 and Na_2O content (0.49–2.11 wt% and 0.56–1.86 wt%, respectively) than Group A websterites (0.09–0.94 wt% and 0.54–1.19

wt%, respectively). The clinopyroxene compositions show a progressive trend of decreasing TiO_2 and Na_2O and increasing CaO with increasing Mg# from Group A to Group B websterites.

5.4. Spinel

The spinel is aluminous (Al_2O_3 >47.1 wt%) having a relatively low Cr_2O_3 content (Cr_2O_3 <10.7 wt%). The Mg# and Al_2O_3 contents of spinel decrease progressively from Group A (68.2–88.6 and 56.5–68.6 wt%, respectively) to Group B websterites (42.4–75.6 and 47.1–60.6 wt%, respectively). The Cr# (= 100 × Cr/[Cr+Al] in mole fractions) is always <11.3 with the highest values for the Group A websterite sample 12Th (5.6–11.3) (Fig. 4). TiO_2 content is <0.86 wt% and the highest concentrations are observed in Group B websterites (0.16–0.86 wt%). The spinel in amphibole-garnet-plagioclase websterite IT26 (Group B) is characterized by higher TiO_2 (0.45–0.86 wt%) and Mg# (42.35–48.85). The exsolution lamellae in spinel from sample IT23 (Group B) are characterized by higher TiO_2 (0.7 wt%) and FeO (32.34 wt%) and a lower Al_2O_3 (47.06 wt%) content than other spinel (TiO_2: 0.16–0.25 wt%, FeO: 18.09–19.02 wt%, and Al_2O_3: 58.61–60.59 wt%).

5.5. Plagioclase

We analyzed plagioclase for the spinel-amphibole-garnet websterite IT26 (Group B) only. The plagioclases are usually andesine ($An_{41.7–42.4}$), except for one bytownitic plagioclase ($An_{70.4}$) observed in a small vein.

5.6. Garnet

Garnet compositions in the xenolith suite cover the range Py43–79, Alm3–40, Grs6–23, with a minor spessartine component (<2). All garnet xenoliths are very poor in Cr_2O_3 (<0.42 wt%) and relatively rich in CaO (4.51–8.13 wt%). Cr_2O_3 and Na_2O content increases progressively from Group A (<0.42 wt%,

<0.93 wt%, respectively) to the websterites (0.01–0.3 wt%, 0.02–0.33 wt%, respectively). TiO_2 concentrations are always <0.13 wt%. Garnet from websterites has a relatively homogeneous Al_2O_3 composition (22.28–24.46 wt%), except the one around spinel from sample IT45 that displays a higher Al_2O_3 content (26.49 wt%). The exsolution lamellae in garnet from sample 26Th (Group A) do not present any significant differences from those found in xenomorphic crystals. Although there are no remarkable variations between coronas and garnet crystals, the garnet halos around spinel or sapphirine often show a greater enrichment in Na, Ca, and Al.

5.7. Sapphirine

We observed sapphirine only in Group A websterites from Tel Tannoun and Tel El Ajailate. Sapphirine always appears as coronas around spinel associated (or not) with garnet. All sapphirine stoichiometries fall between two poles: a 2:2:1 (siliceous pole) and 7:9:3 (aluminous pole) in the (Mg,Fe)O Al_2O_3 SiO_2 system (Higgins et al. 1979). The studied sapphirines typically have a composition close to 15:17:7 (Fig. 5). Their chemical composition is normally homogeneous, lacking any systematic variations between those only with spinel and those associated with garnet. Sapphirine has a high Mg# (90.6–94.5) and Al_2O_3 content (55.27–61.51 wt%). All sapphirines have negligible TiO_2 (0.01–0.08 wt%), whereas their Cr_2O_3 content, however, is relatively high (0.51–4.52 wt%).

5.8. Amphibole

Amphiboles occur in two samples of Group B (websterite IT26 and composite xenolith IT41). They are Ti-pargasites, based on the classification of Leake et al. (1997). Their Mg# in websterite IT26 (72.3–90.4) is higher than that in the composite xenolith IT41 (ca. 66.6). The amphiboles are relatively poor in Cr_2O_3 (<0.66 wt%) and K_2O (0.15–1.3 wt%) and rich in Na_2O (2.81–3.62 wt%) and TiO_2 (1.53–4.51 wt%).

6. Trace elements in clinopyroxenes

REE and other trace element concentrations in clinopyroxenes cores are listed in Table 3 and presented in Fig. 6. No trace element data are available for websterites 20Th, 21Th, 26Th, IT23, IT28, and II10. We also subdivided the xenoliths containing clinopyroxenes having variable trace element contents into two groups on the basis of the shape of their REE patterns and their major elements and Sc, V, and Ni. This geochemical-based subdivision agrees well with the mineralogical one.

6.1. Group A

Clinopyroxenes are usually characterized by a low abundance of LREE relative to MREE and HREE (IT2, IT8, IT45, IT53, 9Th, 12Th, 15Th, 16Th, and IG4, Fig. 6). They have a high Mg# (86.3–91.7), high Al_2O_3 (6.32–9.07 wt%), CaO (21.16–23.3 wt%), Cr_2O_3 (0.07–0.96 wt%), Ni (190–440 ppm), and V (175–505 ppm) content and a low Na_2O (0.62–1.12 wt%), TiO_2 (0.01–0.38 wt%), and Sc (20–57 ppm) content (Tables 2 and 3). The $[La/Yb]_N$ (N = primitive mantle–normalized, after McDonough and Sun, 1995) ratios are low and range from 0.07 to 1.16. The clinopyroxenes of this group (Fig. 6) have a shape similar to those of Syrian peridotites depleted in LREE (Ismail et al., 2008) and spinel-garnet pyroxenites from Jordan (Shaw et al., 2007). Clinopyroxenes in the garnet-rich websterite IT53 are distinguished by a lower REE content relative to other xenoliths, whereas those of websterite 12Th are slightly depleted in Eu. The spinel websterite 16Th is characterized by a progressive depletion from Yb to Pr, and in contrast, by a slight enrichment in Ce and La showing a ‘‘spoon-shaped’’ REE pattern ($[La/Sm]_N$: 0.40; $[Sm/Yb]_N$: 0.25; $[La/Yb]_N$: 0.15). Trace element patterns display a marked enrichment in some of the LILE (Th and U for the samples 9Th, 12Th, and 15Th), and Eu (samples 15Th, 16Th, IT2, and IT53) as well as being highly depleted in Ba, Zr, Ti, and Nb (sample 15Th) and Sr for the websterite samples, 9Th and 12Th. Their Sr concentrations are relatively low at 1 to 25 ppm (Fig. 6).

6.2. Group B

Clinopyroxenes are characterized by REE and trace element patterns that show an enrichment in the most incompatible trace elements (IT26, IT41, and II31). They have a low Mg# (67.4–88.4) and a variable Al_2O_3 (2.24–8.73 %), CaO (17.35–23.27 wt%), Cr_2O_3 (< 0.78 wt%), V (230–290 ppm), and Ni (55–255 ppm) content as well as a high Na_2O (0.56–1.86 wt%), TiO_2 (0.49–2.11 %), and Sc (55–75 ppm) content (Table 2 and 6). All clinopyroxenes are highly enriched in REE compared to the primitive mantle (PM; McDonough and Sun, 1995), ranging 1–26× PM values. The clinopyroxenes of samples IT26 and IT41 are very homogeneous and clearly more enriched in REE than the clinopyroxenes of sample II31. Their trace element patterns show regular enrichments from HREE to MREE for websterite II31 and Nd for websterites IT26 and IT41, whereas the LREE are slightly depleted relative to MREE $(La/Sm]_N$: 0.30–0.53; $[Sm/Yb]_N$: 0.98–1.90; and $[La/Yb]_N$: 0.49–1.39. Only the clinopyroxene from the olivine websterite II31 plots within the field of LREE-rich clinopyroxenes from the Syrian mantle peridotites (Ismail et al., 2008) (Fig. 6). The Group B clinopyroxene trace element patterns have negative Ba, Nb, Pb, Sr, Zr, and Ti anomalies and have positive U and Nd anomalies (Fig. 6).

7. Whole rock major and trace element composition

The major and trace element composition of the studied websterite xenoliths are listed in Table 4. These websterites are ultrabasic and basic having a SiO_2 range from 39.81 to 49.57 wt% and a MgO range from 11.52 to 26.50 wt%. The Mg# decreases sharply from Group A (76–90) to Group B (56–84) websterites (Fig. 7). The Group B websterites are characterized by a higher TiO_2 (0.34–2.57 wt%) and FeO_{total} (7.83–18.05 wt%) content than the Group A websterites (TiO_2: 0.05–0.52 wt%, and FeO_{total}: 3.68–10.11 wt%), whereas Group B has the lowest Al_2O_3 concentrations (7.87–16.26 wt%). Mg# is negatively correlated with TiO_2, FeO_{total}, K_2O, and Na_2O from Group A to Group B, reflecting their modal mineralogy, particularly in ilmenite, magnetite, and plagioclase. All websterite xenoliths of Group A and one Group

B olivine websterite IT23 are similar in composition to the "Mafic 1" field defined for global granulite xenoliths (Kempton and Harmon, 1992; Fig. 7). Two spinel-olivine websterites, II10 and II31, from the Group B xenoliths have the highest SiO_2/Al_2O_3 ratios (10.5–11.2), whereas the composite IT41 and spinel-garnet-plagioclase websterite IT26 plot within the "primitive basaltic magma" field. Compatible trace elements, such Cr, Ni, Co, V, and Sc, vary markedly within the xenolith suites. The xenoliths of Group A, particularly spinel-garnet-sapphirine websterites, are characterized by high concentrations of Cr (355–2265 ppm), V (70–215 ppm), and Sc (12–25 ppm), and low Ni (170–210 ppm) and Co (15–20 ppm) (Table 4).

Clinopyroxenes in both groups have distinctive PM–normalized REE patterns (Fig. 8). Within each group, the xenoliths usually exhibit homogeneous trace element compositions. Group A websterite xenoliths commonly show LREE depletion compared to MREE and HREE ($[La/Sm]_N$: 0.35–2.10; $[Sm/Yb]_N$: 0.07–0.55; and $[La/Yb]_N$: 0.09–0.75) (Fig. 8). All xenoliths of this group display a slight enrichment either in La (IT8, 9Th, 12Th, 15Th, 16Th, and 20Th) or La-Ce (IT45, IT53, IT2, 21Th, and 26Th). The garnet-rich websterite IT53 is distinct from the other websterites by having an extremely low LREE abundance, whereas sample IT28 is slightly enriched in HREE and MREE (2× PM). The Group A websterites are greatly depleted in some HFSE (Ti, Zr, and Nb for 9Th, 12Th, IT8, IT28, and IT53) and LILE (Th, Rb, and Sr for 9Th, 12Th, 20Th, and IT28), whereas the samples are enriched in Ba, U, and Pb (except for the sample 16Th) and also show a slight enrichment in Ta.

Group B websterites have upward convex, normalized patterns, enriched in MREE relative to LREE and HREE ($[La/Sm]_N$: 0.35–0.90; $[Sm/Yb]_N$: 0.75–1.55; and $[La/Yb]_N$: 0.45–2.25) (Fig.8). The composite xenolith and one garnet-plagioclase–bearing websterite IT26 have the highest REE abundance (ca. 5× PM). The Group B websterites display positive Ba and U anomalies and negative Zr, Pb, Th, Nb, and Sr anomalies (except for sample IT41). Low Ti content is only observed in two samples, II10 and II31. The

slight Eu enrichment in xenoliths IT26 and IT41 is consistent with the occurrence of plagioclase in these rocks.

8. Sr-Nd isotopic composition

The Sr-Nd isotopic composition of five clinopyroxenes from Group A spinel-garnett±sapphirine websterite xenoliths (IT2, IT8, IT53, 12Th, and IG4) are remarkably heterogeneous in $^{87}Sr/^{86}Sr$ (0.702970–0.706177) and in $^{143}Nd/^{144}Nd$ (0.512953–0.514024). Furthermore, all plot outside the mantle array (Fig. 9). These clinopyroxenes are usually depleted in LREE (Fig. 6) and have low to very low Rb/Sr and Sm/Nd ratios. Clinopyroxenes from samples IG4 and IT2 show an atypical isotopic composition, particularly their relatively high $^{143}Nd/^{144}Nd$ ratios (= 0.513850–0.514024). The clinopyroxene from sample 12Th has the lowest observed radiogenic Sr and Nd isotopic composition ($^{87}Sr/^{86}Sr$ = 0.702970 and $^{143}Nd/^{144}Nd$ = 0.512953) and is similar to the clinopyroxene found in the Arabian lithospheric mantle or in the Syrian mantle xenoliths. The clinopyroxene in the spinel-garnet-sapphirine–bearing websterite IT53 is extremely radiogenic in $^{87}Sr/^{86}Sr$ (0.706177), but it has a very low LREE content and low amounts of highly incompatible elements (Rb, Sr). Its highly radiogenic Sr isotopic signature could be due to recent surface alteration and will not be discussed further. It does, however, have a similar $^{143}Nd/^{144}Nd$ to the clinopyroxene from sample IT8 and clinopyroxenes from the Syrian, Arabian, and Jordanian lithospheric mantle (Fig. 9).

9. Pressure-temperature estimates

We calculated temperatures estimates using the two-pyroxene (clinopyroxene-orthopyroxene) geothermometers of Wells (1977) and Brey and Köhler (1990a), and we calculated pressure estimates using the garsnet-orthopyroene geobarometer of Harley (1984), only considering the major element composition of mineral cores (Table 1). Except for the composite xenolith IT41, the estimated

temperatures and pressures of the websterite xenoliths are relatively similar and range respectively from 885 to 1080 °C and 1.1 to 1.5 GPa. The Brey and Köhler geothermometer (1990a) estimates temperatures of 820–1080 °C, slightly higher than those based on the Wells (1977) geothermometer (815–1050 °C). The temperature estimates in the composite xenolith IT41 are very homogenous and low (815–820 °C at 1.2 GPa), whereas the spinel-olivine–bearing websterite IT23 has a higher estimated temperature of 1050–1080 °C. The temperature estimates for Group B websterites (815–1080 °C) are slightly higher than those estimated for Group A (895–1000 °C). The low temperatures of the spinel-olivine websterites II10 and II31 (885–905 °C) compared to other xenoliths could relate to slight alteration effects. Spinel-garnet websterites, with or without sapphirine, commonly have similar equilibration temperatures in the range 900–1000 °C, irrespective of the applied geothermometers.

Pressures for the spinel-garnet-sapphirine xenoliths (1.2 to 1.5 GPa) are slightly higher than for those lacking sapphirine (1.1 to 1.3 GPa). Pressures cannot be calculated for xenoliths lacking garnet, but they can be deduced approximately from experimental studies, and by comparing mineral assemblages with known phase stability fields. Therefore, we estimated that spinel-olivine xenoliths (IT23, II10, and II31) equilibrated at a pressure range of 1.0 to 1.5 GPa. Based on their mineral assemblages, all studied websterites re-equilibrated in the garnet-pyroxenite stability field, except for the spinel-garnet websterite IT28 (Fig. 10). This latter assemblage lies at the boundary between the spinel and garnet-pyroxenite stability fields; however, the estimated temperature and pressures of this study (950 ± 130 °C and 1.25 ± 0.18 GPa) are slightly lower than those calculated using CO_2 fluid-inclusion microthermometry in mantle pyroxenites (1200 °C and 1.5 GPa) along the Syrian Rift (Bilal and Touret, 2001) and correspond to the estimated average temperature and pressure.

10. Discussion

10.1 An igneous origin for the meta-websterite xenolith suites

Based on the model of Kempton and Harmon (1992) for identifying the origin of granulites (Fig. 7), most xenoliths show a strong affinity with the "Mafic 1" field. The exceptions are two samples having a lower Mg# that are similar to "primitive basaltic melts". The whole-rock Mg# and SiO_2/Al_2O_3 of the xenolith suite are therefore consistent with them being magmatic cumulates of pyroxene and olivine (and/or plagioclase), except for the two amphibole-bearing xenoliths IT26 and IT41. Some of the xenoliths in the suite also show an affinity with high pressure (1.2 GPa) experimental igneous pyroxenites (Fig. 3, Müntener et al. 2001). The spinel composition of the websterite xenoliths clearly differs from that of Syrian mantle xenoliths (Ismail et al., 2008), abyssal peridotites (Dick and Bullen, 1984), and subduction-zone pyroxenites from the Solomon Islands (Berly et al., 2006). Rather, they resemble sapphirine-garnet–bearing oceanic meta-gabbros from the Kerguelen Archipelago (Grégoire, 1994; Grégoire et al., 1998), which have a clear tholeiitic-transitional affinity related to a high degree of partial melting of a depleted mantle source (Fig. 4). All studied Syrian websterites (Fig. 10) have a rather similar equilibration T (900–1100 °C) and P (1–1.5 GPa), comparable to equilibration temperatures and pressures for spinel-bearing mantle xenoliths from the Arabian Plate (McGuire, 1988; Nasir and Safarjalani, 2000; Bilal and Touret, 2001; Bilal and Sheleh, 2004; Nasir et al., 2006; Ismail et al., 2008); the exception is for the composite xenolith (IT41; T: ~820 °C and P: 1.2 GPa). In contrast, the Syrian pyroxenite xenoliths display much higher equilibration temperatures and pressures than the granulite xenoliths from the Arabian Plate (McGuire, 1988; Al-Mishwat and Nasir, 2004), and they crystallized at depths close to the Moho and can be considered as deep magmatic segregates near the crust–lithospheric mantle transition zone.

10.2 Sp±Ga±Sa–bearing websterites (Group A): Deep cumulates from tholeiitic-transitional basaltic melts

Group A xenoliths are characterized by anhydrous parageneses and the occurrence of garnet. Their major element compositions of mineral phases and whole rocks are commonly homogenous. They show a high

Mg#, Al_2O_3, and CaO content as well as low concentrations of TiO_2, Na_2O, K_2O, and P_2O_5. Trace element composition in clinopyroxenes and whole rocks are also homogenous and commonly characterized by low REE, Zr, Ti, Sr, Rb, and Th. However, preferential enrichment in LREE in whole rocks or clinopyroxenes, particularly in La, Ce, and Pr, as well as some very incompatible elements (Fig. 6 and 8), indicates that these cumulates were later metasomatized by small volumes of silicate melt percolating through the upper lithospheric mantle beneath the Syrian Rift. All the clinopyroxenes in the sapphirine-garnet–bearing websterites show similarities with the sapphirine-garnet–bearing oceanic meta-gabbros from the Kerguelen Archipelago equilibrated in the granulite facies (Grégoire, 1994; Grégoire et al., 1998), but are more aluminous than in mantle pyroxenites worldwide, and subduction-zone pyroxenites from the Solomon Islands (Berly et al., 2006) (Fig. 3). The Syrian pyroxenite xenoliths suite (Fig. 5) crystallized at depth close to the Moho and may be considered as deep magmatic segregates around the crust–lithospheric mantle transition zone. The Syrian sapphirines commonly plot in the field of the sapphirine granulites from Antarctica (Dunkley et al., 1999; Harley and Motoyoshi, 2000; Tsunogae et al., 2002; Grew et al., 2006). In detail, some fall within the sapphirine field of basic granulites from the Finero ultrabasic and basic massif (Sills et al., 1983); others are situated within the field of sapphirine-garnet meta-gabbros from the Kerguelen Archipelago (Grégoire 1994, Grégoire et al.,1998) or in the field of sapphirine from ultra-high-temperature granulites from north-central Madagascar (Goncalves, 2002). Only three sapphirines fall within the field of the Indian sapphirine granulites (Mohan et al., 1996; Owen et al., 2003; Braun et al., 2007); however, they are all situated at the boundary of the sapphirine field for the basic granulite xenoliths from Stockdale, USA (Meyer and Brookins, 1976).

The major and trace element composition of Group A xenoliths compares to that of ultramafic and mafic cumulates derived from tholeiitic to tholeiitic-transitional melts of the lithospheric mantle of the Arabian Plate (Al-Mishwat and Nasir, 2004), some ophiolitic complexes of the Apennines from Italy (Cottin, 1984), and Type II xenoliths from the oceanic lithospheric mantle beneath the Kerguelen Archipelago

(Grégoire, 1994; Grégoire et al., 1998). The mineralogical and chemical characteristics suggest that Group A xenoliths represent deep cumulates (1–1.15 GPa) crystallized from basaltic melt that have a tholeiitic to transitional affinity derived from a depleted MORB-source mantle (DMM), similar to the clinopyroxene compositions of some Patagonian mantle xenoliths (Melchiorre et al., 2015).

10.3 Sp±Ol±Pl–bearing websterites (Group B): Deep cumulates from alkali basaltic melts

The olivine±plagioclase±garnet websterites and the composite websterite/anorthosite xenoliths from Group B xenoliths share a similar mineralogical and geochemical composition; this pattern indicates that they are derived from melts being similar in composition. These xenoliths have the highest concentrations of incompatible trace (REE, Zr, Rb, Y, and Sr) and major elements (TiO_2, Na_2O, and K_2O) associated with the lowest Mg#. However, clinopyroxenes in the composite websterite-anorthosite xenolith are relatively similar to garnet-granulites from Saudi Arabia (Fig. 3, McGuire and Stern, 1993). The REE clinopyroxene patterns of Group B are similar in shape to those of spinel-garnet–bearing pyroxenites from the Jordanian lithospheric mantle, but the Group B samples have a higher trace element content (Fig. 6). The two amphibole-bearing websterites, IT26 and IT41, are comparable to olivine clinopyroxenites from the Kerguelen Archipelago (Fig. 8) (Scoates et al. 2008). The enrichment in Ti and alkalis, together with the overall REE enrichment in xenoliths of this group—particularly in MREE—could indicate they are associated with (earlier) alkaline Cenozoic magmatism along the Syrian Rift. This hypothesis is favored by the high REE content of basalts from the same location (Fig. 8; Jabel El Arab, Ismail, 2008). The mineralogical and chemical composition of Group B xenoliths indicates that they could represent deep cumulates crystallized from alkali basaltic melt under HP-HT conditions of the upper lithospheric mantle beneath the Syrian Rift (1.1–1.3 GPa). Finally, all studied websterite xenoliths lacked similarity with Cenozoic alkali basalts from southern Syria (Ismail 2008), indicating

that the slight interaction with basaltic magma observed for some samples could be considered as a minor metasomatic imprint.

10.1. Isotope characteristics of Group A websterites

The measured Sr-Nd isotopic compositions of clinopyroxenes in the websterite suite vary highly, especially in terms of the $^{143}Nd/^{144}Nd$ isotopes (Table 5); however, these clinopyroxenes also have low Rb/Sr and $^{147}Sm/^{144}Nd$ values. Their measured isotopic composition cannot have changed significantly since the originating eruption (<10 Ma). The age of the websterite formation being unknown, the initial Sr-Nd isotopic ratios of the websterite cannot be used to discuss the exact nature of the mantle source from which they formed. Clinopyroxenes in the Sp-Ga-Sa–bearing websterite 12Th and the spinel-garnet–bearing websterite IT8 have Sr-Nd isotopic ratios comparable to clinopyroxenes from the Arabian lithospheric mantle or from Saudi Arabian and Jordanian mantle xenoliths but different from those of the Afar plume field (Fig. 9). They also have similar Sr-Nd isotopic ratios to clinopyroxene from Syrian mantle xenoliths. Except for sample IT53, which has a very radiogenic Sr isotopic ratio (0.706177, Table 5), all clinopyroxenes have Sr isotopic ratios in the range of those for southern Syrian alkaline basalts, and all have Sr and Nd isotopic compositions that differ from those found in Jordanian pyroxenites and in the upper crust of the Arabian Plate (Fig. 9). The Nd isotopes of these four samples vary quite markedly, while Sr isotopes present a relatively limited variation; this pattern is similar to that of clinopyroxene from the Syrian, Saudi Arabian, and Jordanian mantle xenoliths. Depleted mantle Nd-model ages (T_{DM}) for two websterites are younger (140–250 Ma, Table 5) than the large range of T_{DM} of 270–910 Ma given for the formation of Jordanian mantle peridotites by Shaw et al. (2007). The highly radiogenic Nd isotopic ratios and the associated respective T_{DM} model ages of 515 and 717 Ma (IG4 and IT2) could reflect their derivation from an older portion of lithospheric mantle beneath the Arabian Plate, structured during the pan-African orogeny (750–620 Ma) as also suggested by other studies (McGuire

and Stern, 1993; Brooker et al., 2004; Shaw et al., 2007). The pyroxenite xenoliths could thus represent ancient cumulates, formed possibly at the time of the pan-African orogeny or later when such lithospheric domains were reactivated by later tectonic events, such as rifting and intracontinental extension (620–530 Ma) along the northern edge of the Arabian Plate (Husseini, 1989; Brueckner et al., 1995; Blusztajn et al., 1995; Shaw et al., 2007). The highly variable T_{DM} in clinopyroxenes supports the idea that the northern border of the Arabian lithosphere in Syria and Jordan is composed of mantle portions that were extracted or reworked at different times during important geodynamic events that have structured the Arabian Plate since pan-African times.

10.2. Structure of the lower crust and upper mantle beneath the Syrian Rift

Thermobarometric data for the studied websterites (Fig. 10) indicate that the xenoliths were derived from deep levels within the lithosphere (~28–44 km). These thermobarometric estimations can be correlated with seismic discontinuities observed beneath the Syrian Rift. The seismic and gravity models suggest that the thickness of the crust in Syria is about 37 km (McBride et al., 1990; Sawaf et al., 1993; Brew et al., 2001a). Geophysical studies coupled with those of mantle xenoliths from the northwestern part of the Arabian Plate (Syria, Jordan and Saudi Arabia) indicate that the lithosphere-asthenosphere boundary occurs at a depth ranging between 70 and 75 km (Gettings et al., 1986; El-Isa et al., 1987a, b; McGuire and Bohannon, 1989; McBride et al., 1990; Sawaf et al., 1993; Hofstetter and Bock, 2004; Al- Damegh et al., 2005). Four major seismic discontinuities are distinguished in the northwestern region of the Arabian Plate on the basis of seismic data (El-Isa et al., 1987a, b; McBride et al., 1990; Sawaf et al., 1993; Brew et al., 2001a, b; Al-Damegh et al., 2005). The first discontinuity is situated at a depth between 19 and 21 km and represents the transition zone between upper crustal granitic and meta-volcanic rocks (Vp = 6.2 km s^{-1}) and deeper mafic rocks (Vp = 6.7 km s^{-1}) of the Arabian Shield. Gabbros having tholeiitic, tholeiitic-transitional, and alkaline affinities also occur in Cretaceous (Jubats region) and

Neogene–Quaternary (Tel Tannoun locality) rocks and may represent such a deeper mafic crustal level (Ismail, 2008). The second discontinuity can be found at a depth between 27 and 30 km and corresponds to a thick crust-mantle transition zone. It is characterized by an increase in P-wave velocity (from Vp = 7.1 km s^{-1} to Vp = 7.7 km s^{-1}) and a thickness varying between 5 and 8 km. The third discontinuity represents the true Moho at a depth of 35–40 km, similar to the depth range for the studied xenoliths as deduced from equilibrium pressure calculations (Table 1). The comparison between geophysical and petrological data indicates that the investigated Syrian pyroxenite xenolith suite likely represents deep ultramafic and mafic segregates constitutive of the petrological Moho beneath the Syrian Rift. A similar interpretation has been proposed for oceanic granulite xenoliths from the Kerguelen Archipelago in a mantle plume context (Grégoire et al., 1998), as well as various continental orogenic settings, including the late Hercynian Ivrea area in the Alps (Garuti et al., 2001) or the Caledonian subcrustal delamination domain of the sub-Scottish area, revealed by xenoliths and attesting to the opening of the Iapetus Ocean following the breakup of the Rodinia supercontinent (Halliday et al., 1993; Downes et al., 2001, Bonadiman et al., 2008, Upton et al., 2011). The ultramafic segregates of various affinities in the Syrian xenoliths could have formed as dikes or lenses within the lherzolitic or harzburgitic mantle in a continental or oceanic setting (Wilshire and Shervais, 1975; Grégoire et al., 1998). We suggest that these pyroxenites may represent the subhorizontal boundary between the Syrian lithospheric upper mantle, where underplated tholeiitic-transitional melts intruded at the base of a thinned Syrian crust in response to Mesozoic rifting, and magmatism beneath the Arabian Plate (Stein and Hoffman 1992) and the eastern Mediterranean region. This scenario may also be supported by the occurrence of early Mesozoic ophiolites (Parot 1977, 1980, Dileck et al., 1991). The alkaline ultramafic-mafic cumulates could also represent deep dikes or lenses also associated with the Mesozoic rifting episode in Syria, itself possibly related to a “fossilized?” Cretaceous mantle plume head (Stein and Hoffman 1992). The small number of old Nd-model ages of some tholeiitic-transitional cumulates also suggests their formation may be

linked to older geodynamic events that structured the Arabian Plate during the pan-African period (Shaw et al., 2007).

11. Conclusions

The Cenozoic alkali basalts of Jabel El Arab (Harat Ash Shamm) from southern Syria carry anhydrous websterite xenoliths. The sapphirine coronas, described in some xenoliths, are a main characteristic feature of some of the Syrian spinel-garnet–bearing websterites and attest to the reaction from spinel+orthopyroxene+anorthite to clinopyroxene+garnet+sapphirine. The pyroxenite suite can be divided into two groups based on petrographical, mineralogical, and geochemical composition:

- Group A consists of deep magmatic cumulates (1–1.5 GPa) crystallized from basaltic liquids of **tholeiitic-transitional** affinity that originated from a depleted mantle source.
- Group B consists of deep magmatic cumulates that crystallized under HP-HT conditions (1.2–1.5 GPa) from liquids of **alkaline** affinity.

The high Mg# and high Al_2O_3 and CaO content coupled with low SiO_2/Al_2O_3 ratios indicate the cumulative origin of the xenolith suite under high-pressure conditions. The xenoliths have been equilibrated in the garnet-pyroxenite stability field (950 ± 130 °C and 1.25 ± 0.18 GPa), indicating that they were derived from the crust and lithospheric mantle transition zone at an approximate depth between 28 and 44 km. Nd isotopic ratios of the lithospheric mantle beneath the Syrian Rift vary greatly. Based on a limited number of Nd-model ages and considering the geodynamic history of the Arabian Plate, we propose that tholeiitic-transitional and alkaline magmas were underplated below or intruded at the base of a thinned Syrian crust in response to Mesozoic rifting and magmatism beneath the Arabian Plate and the eastern Mediterranean region.

Acknowledgments

This publication is part of M. Ismail's Ph.D. thesis, work that was supported by UMR CNRS 6524 "Magmas et Volcans". The authors thank F. Sheleh, A. Bilal, and J. Touret who provided some of the samples for this study and Peter Bowden and Chris Harris for revising the English language of an earlier version of this manuscript. We are grateful to Osman Candan and Massimo Coltorti for their very constructive reviews.

References

Adiyaman O, Chorowicz J (2002) Late Cenozoic tectonics and volcanism in the northwestern corner of the Arabian Plate: a consequence of the strike-slip Dead Sea Fault Zone and lateral escape of Anatolia. Journal of Volcanology and Geothermal Research, 117: 327-345.

Al-Damegh K, Sandvol E, Barazangi M (2005) Crustal structure of the Arabian Plate: new constraints from the analysis of teleseismic receiver functions. Earth Planet Science Letters,, 231: 177-196.

Al-Fugha H, AL-Amaireh M (2007) Petrology and origin of ultramafic xenoliths from north-eastern Jordan volcanoes. American Journal of Applied Sciences, 4: 491-495.

Al-Mishwat AT, Nasir SJ (2004) Composition of the lower crust of the Arabian Plate: a xenolith perspective. Lithos, 72: 45-48.

Al-Safarjalani A, Nasir S, Fockenberg T, Massonne HJ (2009) Chemical composition of crustal xenoliths from southwestern Syria: Characterization of the upper part of the lower crust beneath the Arabian Plate. Chemie der Erde Geochemistry, 69, 359-375.

Asfahan J. (2011) Basalt characterization by means of nuclear and electrical well logging techniques. Case study from Southern Syria. In Atomic Energy Commission, Damascus, Syria. Radiation and Isotopes, 69: 641–64.

Baker JA, Menzies MA, Thirlwall MF, Macpherson CG (1997) Petrogenesis of Quaternary intraplate volcanism, Sana'a, Yemen; implications for plume-lithosphere interaction and polybaric melt hybridization. Journal of Petrology, 38: 1359-1390.

Baker JA, Chazot G, Menzies MA, Thirlwall MF (1998) Metasomatism of the shallow mantle beneath Yemen by the Afar plume-implications for mantle plumes, flood volcanism and intraplate volcanism. Geology, 26: 431-434.

Berly TJ, Hermann J, Arculus RJ, Lapierre H (2006) Supra-subduction zone pyroxenites from San Jorge and Santa Isabel (Solomon Islands). Journal of Petrology, 47: 1531-1555.

Bertrand H, Chazot G, Blichert-Toft J, Thoral S (2003) Implications of widespread high-μ volcanism on the Arabian Plate for Afar mantle plume and lithosphere composition. Chemical Geology, 198: 47-61.

Beydoun ZR (1991) Arabian Plate hydrocarbon geology and potential a plate tectonic approach. American Association of Petroleum Geologists, Studies in Geology 33: 77 pp.

Bilal A, Touret JLR (2001) Les enclaves du volcanisme récent du rift Syrien. Bulletin Société Géologique de France, 172: 1-14.

Bilal A, Sheleh F (2004) Un «point chaud» sous le système du rift Syrien: données pétrologiques complémentaires sur les enclaves du volcanisme récent. Comptes Rendus Geosciences, 366: 197-204.

Blusztajn J, Hart SR, Shimizu N, McGuire AV (1995) Trace-element and isotopic characteristics of spinel peridotite xenoliths from Saudi Arabia. Chemical Geology, 123: 53-65.

Bodinier JL, Guiraud M, Fabriès J, Dostal J, Dupuy C (1987) Petrogenesis of layered pyroxenites from the Lherz, Freychinède and Prades ultramafic bodies (Ariège, French Pyrénées). Geochimica et Cosmochimica Acta, 51: 279-290.

Bodinier JL, Dupuy C, Dostal J (1988) Geochemistry and petrogenesis of Eastern Pyrenean peridotites. Geochimica et Cosmochimica Acta, 52: 2893-2907.

Bohannon RG, Naeser CW, Schmidt DL, Zimmermann RA (1989) The timing of uplift, volcanism, and rifting peripheral to the Red Sea; a case for passive rifting? Journal of Geophysical Research, 94: 1683-1701.

Bonadiman C, Coltorti M, Duggen S, Paludetti L, Siena F, Thirlwall IMF, Upton BGJ (2008) Paleozoic subduction related and kimberlite or carbonatite metasomatism in the Scottish lithospheric mantle. In, Coltorti M and Grégoire M. eds. Metasomatism in oceanic and continental lithospheric mantle; Geological Society London Special Publication 293: 303-333.

Braun I, Cenki-Tok B, Paquette JL, Tiepolo M (2007) Petrology and U-Th-Pb geochronology of the sapphirine-quartz-bearing metapelites from Rajapalayam, Madurai Block, southern India: evidence for polyphase Neoproterozoic high-grade metamorphism. Chemical Geology, 241: 129-147.

Brew G, Barazangi M, Al-Maleh AK, Sawaf T (2001a) Tectonic and geologic evolution of Syria. GeoArabia Journal, 6: 573-616.

Brew G, Lupa J, Barazangi M, Sawaf T, Al-Imam A, Zaza T (2001b) Structure and tectonic development of the Ghab Basin and the Dead Sea Fault System, Syria. Journal of the Geological Society of London, 158: 665-674.

Brey GP, Köhler TK (1990a) Geothermobarometry in four phase lherzolites I. Experimental results from 10 to 60 kb. Journal of Petrology, 31: 1313-1352.

Brooker RA, James RH, Blundy JD (2004) Trace elements and Li isotope systematics in Zabargad peridotites: evidence of ancient subduction processes in the Red Sea mantle. Chemical Geology, 212: 179-204.

Brueckner HK, Elhaddad MA, Hamelin B, Hemming S, Kröner A, Reisberg L, Seyler M (1995) A Pan-African origin and uplift for the gneisses and peridotites of Zabargad Island, Red Sea: a Nd, Sr, Pb, and Os isotope study. Journal of Geophysical Research, 100: 22283-22297.

Camp VE, Roobol MJ (1989) The Arabian continental alkali basalt province: part I. Evolution of Harrat Rahat, Kingdom of Saudi Arabia. Geological Society of America Bulletin, 101: 71-95.

Chorowicz J, Dhont D, Ammar O, Rukieh M, Bilal A (2005) Tectonics of the Pliocene Homs basalts (Syria) and implications for the Dead Sea Fault Zone activity. Journal of the Geological Society of London, 162: 259-271.

Cottin JY (1984) Les gabbros filoniens recoupant les lherzolites à spinelle et plagioclase du Bracco (Apennins-Ligure, Italie). Bulletin Société Géologique de France, 5: 935-944.

Deniel C, Vidal P, Coulon C, Vellutini PJ, Piguet P (1994) Temporal evolution of mantle sources during continental rifting: The volcanism of Djibouti (Afar). Journal of Geophysical Research, 99: 2853-2869.

Dick HJB, Bullen T (1984) Chromian spinel as a petrogenetic indicator in abyssal and alpine-type peridotites and spatially associated lavas. Contributions to Mineralogy and Petrology, 86: 54-76.

Downes H, Upton BGJ, Handisyde E, Thirilwall MF (2001) Geochemistry of mafic and ultramafic xenoliths from Fidra (Southern Uplands, Scotland): implications for lithospheric processes in Permo-Carboniferous times. Lithos, 58: 105-124.

Dubertret L (1933) Les grandes nappes basaltiques Syriennes : âge et relations avec la tectonique, C. R. somme. Bulletin Société Géologique de France, 3: 178-180.

Dunkley DJ, Clarke GL, Harley SL (1999) Diffusion metasomatism in silica-undersaturated sapphirine-bearing granulite from Rumdoodle Peak, Framnes Mountains, east Antarctica. Contributions to Mineralogy and Petrology, 134: 264-276.

El-Isa Z, Mechie J, Prodehl C (1987a) Shear velocity structure of Jordan from explosion seismic data. Geophysical Journal Research Australia Society, 90: 265-281.

El-Isa Z, Mechie J, Prodehl C, Makris J, Rihm R (1987b) A crustal structure study of Jordan derived from seismic refraction data. Tectonophysics, 138: 235-253.

Fabriès J, Lorand JP, Bodinier JL, Dupuy C (1991) Evolution of the upper mantle beneath the Pyrenees: Evidence from orogenic spinel lherzolite massifs. Journal of Petrology, Special Volume on Orogenic Lherzolite and Mantle Processes, 55-76.

Frey FA, Prinz M (1978) Ultramafic inclusions from San Carlos, Arizona. Petrologic and geochemical data bearing on their petrogenesis. Earth and Planetary Science Letters, 38: 1023-1054.

Garrido CJ, Bodinier JL (1999) Diversity of mafic rocks in the Ronda peridotite: evidence for pervasive melt-rock reaction during heating of subcontinental lithosphere by upwelling asthenosphere. Journal of Petrology, 40: 729-754.

Garuti G, Bea F, Zaccarini F, Montero P (2001) Age, geochemistry and petrogenesis of the ultramafic pipes in the Ivrea zone, NW Italy. Journal of Petrology, 42: 433-457.

Gettings ME, Blank JRHR, Mooney WD, Healy JH (1986) Crustal structure of southwestern Saudi

Arabia. Journal of Geophysical Research, 91: 6491-6512.

Goncalves P (2002) Pétrologie et géochimie des granulites de ultra-hautes températures de l'unité basique d'Andriamena (Centre-Nord Madagascar). Apport de la géochronologie in-situ U-Th-Pb à l'interprétation des trajets P-T. PhD Thesis, Université Clermont Ferrand, 320 pp.

Grégoire M (1994) Pétrologie des enclaves ultrabasiques et basiques des Îles Kerguelen (T.A.A.F). Les contraintes minéralogiques et thermobarométriques et leurs implications géodynamiques. PhD Thesis, Université Jean Monnet, Saint Etienne, 253 pp.

Grégoire M, Mattielli N, Nicollet C, Cottin JY, Leyrit H, Weis D, Shimizu N, and Giret A (1994). Oceanic mafic granulite xenoliths from the Kerguelen archipelago. Nature, 367: 360-367.

Grégoire M, Cottin JY, Giret A, Mattielli N, Weis D (1998) The metaigneous xenoliths from Kerguelen Archipelago: evidence of a continent nucleation in an oceanic setting. Contributions to Mineralogy and Petrology, 133: 259-283.

Grégoire M, Mc Innes BIA, O'Reilly SY (2001) Hydrous metasomatism of oceanic sub-arc mantle, Lihir, Papua New Guinea: Trace element characteristics of slab-derived hydrous fluids. Lithos, 59: 91-108.

Grégoire M, Bell DR, Le Roex AP (2002) Trace element geochemistry of phlogopite-rich mafic mantle xenoliths: their classification and their relationship to phlogopite-bearing peridotite and kimberlites revisited. Contributions to Mineralogy and Petrology, 142: 603-625.

Grew ES, Yates MG, Shearer CK, Hagerty JJ, Sheraton JW, Sandiford M (2006) Beryllium and other trace elements in paragneisses and anatectic veins of the ultrahigh-temperature Napier Complex, Enderby Land, East Antarctica: the role of sapphirine. Journal of Petrology, 47: 859-882.

Griffin WL, O'Reilly SY, Stabel A (1988) Mantle metasomatism beneath Western Victoria, Australia. II. Isotopic geochemistry of Cr-diopside lherzolites and Al-augite pyroxenites. Geochimica et Cosmochimica Acta, 52: 449-459.

Haase KM, Muehe R, Stoffers P (2000) Magmatism during extension of the lithosphere; geochemical constraints from lavas of the Shaban Deep, northern Red Sea. Chemical Geology, 166: 225-239.

Halliday AN, Dickin AP, Hunter RH, Davies GR, Dempster TJ, Hamilton PJ, Upton BGJ (1993) Formation and composition of lower continental crust: evidence from Scottish xenoliths suites. Journal of Geophysical Research, 98: 581-607.

Harley SL (1984) An experimental study of the partitioning of the Fe and Mg between garnet and orthopyroxene. Contributions to Mineralogy and Petrology, 86: 359-373.

Harley SL, Motoyoshi Y (2000) Al zoning in orthopyroxene in a sapphirine quartzite: evidence for >1120 $^{\circ}$C UHT metamorphism in the Napier Complex, Antarctica, and implications for the entropy of sapphirine. Contributions to Mineralogy and Petrology, 138: 293-307.

Henjes-Kunst F, Altherr R, Baumann A (1990) Evolution and composition of the lithospheric mantle underneath the western Arabian Peninsula: constraints from Sr-Nd isotope systematics of mantle

xenoliths. Contributions to Mineralogy and Petrology, 105: 460-472.

Herzberg CT (1978) Pyroxene geothermometry and geobarometry; experimental and thermodynamic evaluation of some subsolidus phase relations involving pyroxenes in the system CaO-MgO-Al_2O_3-SiO_2. Geochimica et Cosmochimica Acta, 42: 945-958.

Higgins JB, Ribbe PH, Herd RK (1979) Sapphirine: I. Crystal chemical contributions. Contributions to Mineralogy and Petrology, 68: 349-356.

Hirschmann MM and Stolper EM (1996) A possible role for garnet pyroxenite in the origin of the 'garnet signature' in MORB. Contributions to Mineralogy and Petrology, 124: 185-208.

Hofstetter A, Bock G (2004) Shear-wave velocity structure of the Sinai sub-plate from receiver function analyses. Geophysical Journal International, 158: 67-84.

Husseini M (1989) Tectonic and deposition model of late Precambrian-Cambrian Arabian and adjoining plates. American Association of Petroleum Geologist Bulletin, 73: 1117-1131.

Jarrar G, Stern RJ, Saffarini G, Al-Zubi H (2003) Late- and postorogenic Neoproterozoic intrusions of Jordan: implications for crustal growth in the northernmost segment of the East African Orogen. Precambrian Research, 123: 295-319.

Irving AJ (1974) Geochemical and high-pressure experimental studies of garnet pyroxenite and pyroxene granulite xenoliths from the delegate basaltic pipes, Australia. Journal of Petrology, 15: 1-40.

Irving AJ (1980) Petrology and geochemistry of composite ultramafic xenoliths in alkalic basalts and implications for magmatic processes within the mantle. American Journal of Sciences, 280A: 389-426.

Ismail M (2008) Etude minéralogique et géochimique des enclaves ultramafiques et mafiques du volcanisme Néogène-Quaternaire lié au rift syrien. PhD Thesis, Université Jean Monnet, 446 pp.

Ismail M, Delpech G, Cottin JY, Grégoire M, Moine BN, Bilal A (2008) Petrological and geochemical constraints on the composition of the lithospheric mantle beneath the Syrian rift, northern part of the Arabian Plate. Journal of Geological Society of London, Special Publication, 293: 223-251.

Ito K, Kennedy GC (1971) An experimental study of the basalt-garnet granulite-eclogite transition. The structure and physical properties of the Earth's crust. Geophysical Monograph Series, 14: 303-314.

Kempton PD, Harmon RS (1992) Oxygen isotope evidence for large scale hybridisation of the lower crust during magmatic under-plating. Geochimica et Cosmochimica Acta, 56: 971-986.

Kornprobst J (1969) Le massif ultrabasique des Beni Bouchera (Rift Interne, Maroc): étude des péridotites de haute température et de haute pression, et des pyroxénolites, à grenat ou sans grenat, qui leur sont associées. Contributions to Mineralogy and Petrology, 23: 283-322.

Krienitz MS, Haase KM, Mezger K, Eckardt V, Shaikh-Mashail MA (2006) Magma genesis and crustal contamination of continental intraplate lavas in northwestern Syria. Contributions to Mineralogy and Petrology, 151: 698-716.

Krienitz MS, Haase KM, Mezger K, Shaikh-Mashail MA (2007) Magma genesis and mantle dynamics

at the Harrat Ash Shamah volcanic field (southern Syria). Journal of Petrology, 48: 1513-1542.

Krienitz MS, Haase KM (2010) - The evolution of the Arabian lower crust and lithospheric mantle-Geochemical constraints from southern Syrian mafic and ultramafic xenoliths. Chemical Geology, 280: 271-283.

Kumar N, Reisberg L, Zindler A (1996) A major and trace element and strontium, neodynium, and osmium isotopic study of a thick pyroxenite layer from the Beni Bousera Ultramafic Complex of northern Morocco. Geochimica et Cosmochimica Acta, 60: 1429-1444.

Laws E, Wilson M (1997) Tectonics and magmatism association with Mesozoic passive continental margin development in the Middle East. Journal of Geological Society of London, 154: 459-464.

Leake BE, Wolley AR, Arps CES, Birch WD, Charles Gilbert M, Krivoichev VG, Linthout K, Laird J, Mandarino J, Marsmith DC, Stephenson NCN, Ungaretti L, Whittaker EJW, Youzhi G (1997) Nomenclature of amphiboles, report of the subcommittee on amphiboles of the international mineralogical association commission on new minerals. Mineral names. Mineralogical Magazine, 61: 295-321.

Lustrino M, Sharkov E (2006) Neogene volcanic activity of western Syria and its relationship with Arabian Plate kinematics. Journal of Geodynamics 42: 115-139.

McBride JH, Barazangi M, Best J, Al-Saad D, Sawaf T, Al-Otri M, Gebran A (1990) Seismic reflection structure of intracratonic Palmyride fold-thrust belt and surrounding Arabian Platform, Syria. American Association of Petroleum Geologists Bulletin, 74: 238-259.

McClusky S, Balassanian S, Barka A et al. (2000) Global positioning system constraints on plate kinematics and dynamics in the eastern Mediterranean and Caucasus. Journal of Geophysical Research 105: 5695-5719.

McDonough WF, Sun SS (1995) The composition of the Earth. Chemical Geology, 120: 223-253.

McGuire AV (1988) Petrology of mantle xenoliths from Harrat al Kishb; the mantle beneath western Saudi Arabia. Journal of Petrology, 29: 73-92.

McGuire AV, Bohannon RG (1989) Timing of mantle upwelling; evidence for a passive origin for the Red Sea Rift. Journal of Geophysical Research B, 94: 1677-1682.

McGuire AV, Stern RJ (1993) Granulite xenoliths from western Saudi Arabia: the lower crust of the late Precambrian Arabian-Nubian Shield. Contributions to Mineralogy and Petrology, 114: 395-408.

McInnes BIA, Grégoire M, Binns RA, Herzig PM, Hannington MD (2001) Hydrous metasomatism of oceanic sub-arc mantle, Lihir, Papua New Guinea: petrology and geochemistry of fluid-metasomatised mantle wedge xenoliths. Earth and Planetary Science Letters, 188: 169-183.

Medaris LG, Syada G (1998) Spinel peridotite xenoliths from the Al Ashaer volcano, Syria: a contribution to the elemental composition and thermal state of subcontinental Arabian lithosphere. International Geology Review, 40: 305-324.

Melchiorre M, Coltorti MM, Gregoire M, Benoit M (2015). Enrichment processes in the Patagonian lithospheric mantle. Mineralogia, Special papers, 43: 67-68.

Mercier JCC, Nicolas A (1975) Texture and fabrics of ultramafic peridotites as illustrated by xenoliths from basalts. Journal of Petrology, 16: 454-487.

Meyer HOA, Brookins DG (1976) Sapphirine, sillimanite and garnet in granulite xenoliths from the Stockdale kimberlite, Kansas. American Mineralogy, 61: 1194-1202

Mohan A, Prakash D, Motoyoshit Y (1996) Decompressional P-T history in sapphirine-bearing granulites from Kodaikanal, southern India. Journal of Southeast Asian Earth Sciences, 14: 231-243.

Mouty M, Delaloye M, Fontingnie D, Piskin O, Wagner JJ (1992) The volcanic activity in Syria and Lebanon between Jurrasic and Actuel. Schweizerische Mineralogische Petrographische Mitteilungen, 72: 91-105.

Müntener O, Kelemen PB, Grove TL (2001) The role of H_2O during crystallization of primitive arc magmas under uppermost mantle conditions and genesis of igneous pyroxenites: an experimental study. Contributions to Mineralogy and Petrology, 141: 643-658

Nasir S (1994) Geochemistry and petrogenesis of Cenozoic volcanic rocks from northwestern part of the Arabian continental alkali basalt province. Africa Geoscience Review, 1: 455-467.

Nasir S, Safarjalani A (2000) Lithospheric petrology beneath the northern part of the Arabian Plate in Syria: evidence from xenoliths in alkali basalts. Journal of African Earth Sciences, 30: 149-168.

Nasir S, Safarjalani A (2002) Lithospheric petrology and geochemistry beneath the northern part of the Arabian Plate (Syria). Journal of African Earth Sciences, 34: 223-245.

Nasir S, Al-Sayigh A, Alharthy A, Al-Lazki A (2006) Geochemistry and petrology of Tertiary volcanic rocks and related ultramafic xenoliths from the central and eastern Oman Mountains. Lithos, 90: 249-270.

Nasir S and Rollinson H (2008) The nature of the subcontinental lithospheric mantle beneath the Arabian Shield: mantle xenoliths from southern Syria. Precambrian Research, 172(3-4): 323-333.

Nasir S, Stern RJ (2012) Lithospheric petrology of the eastern Arabian Plate: constraint from Al-Ashkhara (Oman) xenoliths. Lithos, 132-133; 98-112

O'Neill HSC (1981) The transition between spinel lherzolite and garnet lherzolite and its use as a geobarometer. Contributions to Mineralogy and Petrology, 77: 185-194.

Owen JV, Longstaffe FJ, Greenough JD (2003) Petrology of sapphirine granulite and associated sodic gneisses from the Indian Head Range, Newfoundland. Lithos, 68: 91-114.

Parot JF (1977) Ophiolites du Nord-Ouest syrien et évolution de la croûte océanique Téthysienne au cours du mésozoïque. Tectonophysics, 41: 251-268.

Parot JF (1980) The Baër Bassit (Northern Syria) ophiolitic area. *In* Ofioliti, special issue Tethian ophiolites Vol 2 Eastern, p.279

Pearson DG, Davies GR, Nixon PH (1993) Geochemical constraints on the petrogenesis of diamond facies pyroxenites from the Beni Bousera peridotite massif, north Morocco. Journal of Petrology, 34: 125-172.

Piccardo GB, Messiga B, Vannucci R (1988) The Zabargad peridotite-pyroxenite association: petrological constraints on its evolution. Tectonophysics, 150: 135-162.

Rivalenti G, Mazzucchelli M, Vanucci R, Hofmann AW, Ottolini L, Bottazzi P, Obermiller W (1995) The relationship between websterite and peridotite in the Balmuccia peridotite massif (NW Italy) as revealed by trace element variations in clinopyroxene. Contributions to Mineralogy and Petrology, 121: 275-288.

Sawaf T, Al-Saad D, Gebran A, Barazangi M, Best A, Chaimov T (1993) Stratigraphy and structure of eastern Syria across the Euphrates depression. Tectonophysics, 230: 267-281.

Scoates JS, Weis D, Franssens M, Mattielli N, Annelli H, Frey FA, Nicolaysen K, Giret A (2008) The Val Gabbro plutonic suite: a sub-volcanic intrusion emplaced at the end of flood basalt volcanism on the Kerguelen archipelago. Journal of Petrology, 49: 79-105.

Schilling JG, Kingsley RH, Hanan BB, McCully BL (1992) Nd-Sr-Pb isotopic variations along the Gulf of Aden; evidence for Afar mantle plume-continental lithosphere interaction. Journal of Geophysical Research, 97: 927-966.

Seyler M, Mattson PH (1993) Gabbroic and pyroxenite layers in the Tinaquillo, Venezuela, peridotite: succession of melt intrusions in a rising mantle diapir. Journal of Geology, 101: 501-511.

Sharkov EV, Laz'ko Y, Hanna S (1993) plutonic xenoliths from the Nabi Matta explosive center, northwest Syria. Geochemistry International, 30: 23-44.

Shaw JE, Baker JA, Menzies MA, Thirlwall MF, Ibrahim KM (2003) Petrogenesis of the largest intraplate volcanic field on the Arabian Plate (Jordan): a mixed lithosphere-asthenosphere source activated by lithospheric extension. Journal of Petrology, 44: 1657-1679.

Shaw JE, Baker JA, Kent AJR, Ibrahim, KM, Menzies MA (2007) The geochemistry of the Arabian lithospheric mantle a source for intraplate volcanism? Journal of Petrology, 48: 1495-1512.

Shervais JW (1990) Island arc ocean crust ophiolites: contrasts in the petrology, geochemistry and tectonic style of ophiolite assemblages in the California Coast Ranges. In: Malpas J, Moores EM, Panayiotou A, Xenophontos C. (eds) Ophiolites: Oceanic Crustal Analogues. Proceedings of the Symposium 'Troodos 1987'. Nicosia: Geological Survey Department, p. 507-520.

Sills JD, Ackermand D, Herd RK, Windley DF (1983) Bulk composition and mineral parageneses of sapphirine-bearing rocks along a gabbro-lherzolite contact at Finero, Ivrea Zone, northern Italy. Journal of Metamorphic Geology, 1: 337-353.

Sinigoi S, Comin-Chiaramonti P, Alberti AA (1980) Phase relations in the partial melting of the Baldissero spinel-lherzolite (Ivrea-Verbano Zone, Western Alps, Italy). Contributions to Mineralogy and Petrology, 75: 111-121.

Stein M, Hofman AW (1992) Fossil plume head beneath the Arabian lithosphere? Earth and Planetary Science Letters, 114: 193-209.

Stein M, Garfunkel Z, Jagoutz E (1993) Chronothermometry of peridotitic and pyroxenitic xenoliths; implications for the thermal evolution of the Arabian lithosphere. Geochimica et Cosmochimica Acta, 57: 1325-1337.

Stern RJ, Johnson P. (2010) Continental lithosphere of the Arabian Plate: A geologic, petrologic, and geophysical synthesis. Earth Science Reviews, 101: 29-67.

Tsunogae T, Santosh M, Osanai Y, Owada M, Toyoshima T, Hokada T (2002) Very high-density carbonic fluid inclusions in sapphirine-bearing granulites from Tonagh Island in the Archean Napier Complex, east Antarctica: implications for CO_2 infiltration during ultrahigh-temperature (T >1100 °C) metamorphism. Contributions to Mineralogy and Petrology, 143: 279-299.

Upton BGJ, Downes H, Kirstein LA, Bonadiman PG, Hill PG, Ntaflos TN (2011) The lithospheric mantle and lower crust-mantle relationships under Scotland: a xenolithic perspective. Journal of the Geological Society, 168, 873-886.

Vaselli O, Downes H, Thirlwall M, Dobosi C, Coradossi N, Seghedi I, Szakacz A, Vannucci R (1995) Ultramafic xenoliths in Plio-Pleistocene alkali basalts from the Eastern Transylvanian Basin: depleted mantle enriched by vein metasomatism. Journal of Petrology, 36: 23-53.

Volker F, McCulloch MT, Altherr R (1993) Submarine basalts from the Red Sea: new Pb, Sr and Nd isotopic data. Geophysical Research Letters, 20: 927-930.

Weinstein Y, Navon O, Altherr R, Stein M (2006) The role of lithospheric mantle heterogeneity in the generation of Plio-Pleistocene alkali basaltic suites from NW Harrat Ash Shaam. Journal of Petrology, 47: 1017-1050.

Wells PRA (1977) Pyroxene thermometry in simple and complex system. Contributions to Mineralogy and Petrology, 62: 129-139.

Wilshire HG, Shervais JW (1997) Al-augite and Cr-diopside in ultramafic xenoliths from the western United States. Physics and Chemistry of the Earth Journal, 9: 257-272.

Wilkinson JFG, Stolz AJ (1997) Subcalcic clinopyroxenites and associated ultramafic xenoliths in alkali basalt near Glen Innes, northeastern New South Wales, Australia. Contribution to Mineralogy and Petrology, 127: 272-291.

Zanetti A, Mazzucchelli M, Rivalenti G, Vannucci R (1999) The Finero phlogopite peridotite massif: an example of subduction-related metasomatism. Contributions to Mineralogy and Petrology, 134: 107-122

Figure captions

Fig. 1 Geological map of the Syrian Rift showing the websterite xenolith localities at Tel Tannoun, Tel Imtan El Koudre, and Tel El Ajailate, Syria. These sites had eruptions at the surface during Cenozoic basaltic volcanism at Jabel El Arab.

Fig. 2 Photomicrographs of petrographic features in the Syrian websterite xenoliths. (**a**) Spinel enclosing orthopyroxene grains and surrounded by garnet coronas in spinel-garnet–bearing websterite IT28. (**b**) Corona of altered garnet (kelyphite) around spinel in spinel-garnet-sapphire–bearing websterite IG4. (**c**) Garnet and sapphirine coronas around spinel in Ga-Sa–bearing websterite 9Th. (**d**) Composite xenolith of websterite/anorthosite IT41. **e)** Exsolutions of garnet in orthopyroxene grains in Sp-Am-Ga-Pl–bearing websterite IT8. **f)** Mutual exsolutions in orthopyroxene and clinopyroxene in Sp-Ga–bearing websterite IT26. Photomicrographs (**a**) and (**b**) demonstrate that the formation of garnet coronas lacking sapphirine can be explained by the retrograde reaction (**1**) clinopyroxene+orthopyroxene+spinel --> garnet, whereas the garnet and sapphirine corona in photomicrograph (**c**) results from the reaction (**2**) spinel+orthopyroxene+anorthite--> clinopyroxene+garnet+sapphirine.

Fig. 3 Mg# vs Al_2O_3 in clinopyroxenes from Syrian websterite xenoliths. Stars represent data from experimental igneous pyroxenites at 1.2 GPa (Müntener et al., 2001); light gray area represents the compositional field of mantle pyroxenites (Kornprobst, 1969; Irving, 1974, 1980; Frey and Prinz, 1978; Sinigoi et al., 1980; Bodinier et al., 1987, 1988; Griffin et al., 1988; Piccardo et al., 1988; Seyler and Mattson, 1993; Shervais, 1990; Pearson et al., 1993; Rivalenti et al., 1995; Vaselli et al., 1995; Kumar et al., 1996; Wilkinson and Stolz, 1997; Garrido and Bodinier, 1999; Zanetti et al., 1999; McInnes et al., 2001); the dark gray area represents the compositional field of garnet-granulites from Saudi Arabia (McGuire and Stern, 1993); the horizontal lines represent the compositional field of subduction zone pyroxenites from the Solomon Islands (Berly et al., 2006); the horizontal dashed lines represent the

compositional field of spinel of sapphirine-garnet–bearing meta-gabbros from the Kerguelen Archipelago (Grégoire, 1994; Grégoire et al., 1998. Solid circles: spinel-garnet-sapphirine–bearing websterites, open circles: Sp-Ga–bearing websterites, solid squares: spinel-olivine–bearing websterites, open squares: Sp-bearing websterites, solid triangles: spinel-amphibole-garnet-plagioclase–bearing websterite, open triangles: Ga-Am–bearing composite websterite/anorthosite.

Fig. 4 Mg# vs Cr# in spinel from Syrian websterite xenoliths. The light gray area represents the compositional field of spinel from peridotite xenoliths from southern Syria (Ismail et al., 2008); the horizontal dashed lines represent the compositional field of spinel of sapphirine-garnet–bearing meta-gabbros from the Kerguelen Archipelago (Grégoire, 1994); the horizontal lines represent the compositional field of subduction zone pyroxenites from the Solomon Islands (Berly et al., 2006); dark gray area represents the compositional field of abyssal peridotites (Dick and Bullen, 1984). Symbols for rock types are the same as in Figure 3.

Fig. 5 SiO_2+MgO+FeO-Al_2O_3+Cr_2O_3 ternary plot for sapphirine from Syrian websterite xenoliths. Dark gray area represents the compositional field of sapphirine from Indian granulites (Mohan et al., 1996; Owen et al., 2003; Braun et al., 2007); light gray shading represents the compositional field of sapphirine from Antarctic granulites (Dunkley et al., 1999; Harley and Motoyoshi, 2000; Tsunogae et al., 2002; Grew et al., 2006); the vertical line shading represents the compositional field of sapphirine from ultra-high-temperature granulites, north-central Madagascar (Goncalves, 2002); horizontal dashed line shading represents the compositional field of sapphirine of sapphirine±garnet-bearing meta-gabbros from the Kerguelen Archipelago (Grégoire, 1994); the horizontal line shading represents the compositional field of sapphirine from basic granulites of the Finero ultrabasic and basic massif (Sills et al., 1983); the dotted area represents the compositional field of sapphirine from basic granulite xenoliths from Stockdale, USA (Meyer and Brookins, 1976). Symbols for rock types are the same as in Figure 3.

Fig. 6 Primitive mantle-normalized REE and trace element patterns for clinopyroxenes from Syrian websterite xenoliths. Normalized values taken from McDonough and Sun (1995). Dark gray field represents clinopyroxenes of spinel-garnet–bearing pyroxenite xenoliths from Jordan (Shaw et al., 2007); light gray field represents LREE enrichment and depletion patterns for clinopyroxene peridotites from Syria (Ismail et al., 2008, Ismail, 2008). Symbols for rock types are the same as in Figure 3.

Fig. 7 Mg# vs SiO_2/Al_2O_3 diagram after Kempton and Harmon (1992) for Syrian websterite xenoliths compared with fields of global granulite xenoliths (adapted from Grégoire et al., 2001). Symbols for rock types are the same as in Figure 3.

Fig. 8 Primitive mantle–normalized REE and trace element patterns for whole-rock samples of Syrian websterite xenoliths. Normalization values from McDonough and Sun (1995). Light gray and dark gray shading represent respectively Ol-Pl–bearing websterites (Grégoire, 1994; Grégoire et al., 1998) and Ol-bearing clinopyroxenites (Scoates et al., 2008) from the Kerguelen Archipelago, the dark line represents alkali basalt from southern Syria (Ismail, 2008). Symbols for rock types are the same as in Figure 3.

Fig. 9 Measured Sr-Nd isotopic compositions of mantle clinopyroxenes in Syrian websterite xenoliths. Plotted for comparison are the isotopic compositions of Cenozoic Syrian alkali basalts (Bertrand et al., 2003; Krienitz et al., 2006, 2007; Ismail, 2008), Red Sea MORB (Schilling et al., 1992; Volker et al., 1993; Haase et al., 2000), Afar plume (Deniel et al., 1994), Arabian lithosphere mantle (Blusztajn et al., 1995; Baker et al., 1998), upper crust of Arabian Plate (Henger and Pallister, 1989; Jarrar et al., 2003), Saudi Arabian and Jordan mantle xenoliths (Henjes-Kunst et al., 1990; Blusztajn et al., 1995; Brueckner et al., 1995; Shaw et al., 2007), Jordan pyroxenites (Shaw et al., 2007), and Syrian mantle xenoliths (Ismail, 2008). Symbols for rock types are the same as in Figure 3.

Fig. 10 Pressure-temperature estimates for Syrian websterite xenoliths. Geotherm xenoliths of Arabian Plate are modified after Nasir and Safarjalani (2002). Light gray field corresponds to spinel-bearing peridotites of the Arabian Plate (Syria, Jordan, Saudi Arabia, Yemen, and Oman) as determined by McGuire (1988), Nasir and Safarjalani (2000), Bilal and Touret (2001), Bilal and Sheleh (2004), Nasir et al. (2006), Ismail et al. (2008); dark gray field represents granulites from Syria, Jordan, and Saudi Arabia (McGuire, 1988; Al-Mishwat and Nasir, 2004). Spinel lherzolite/garnet lherzolite transitions are from O'Neill (1981). Spinel-pyroxenites/garnet pyroxenites transition is taken from Herzberg (1978) and the olivine-in and garnet-in reactions are from Irving (1974). The dry peridotite solidus is from Ito and Kennedy (1971). Symbols for rock types are the same as in Figure 3.

Table captions

Table 1 Modal composition and calculated equilibration pressures and temperatures of the sampled websterite xenoliths.

Table 2 Representative major element composition (wt%) of minerals within the sampled websterite xenoliths.

Table 3 Trace element composition (ppm) of clinopyroxenes in the sampled websterite xenoliths.

Table 4 Bulk rock major (wt%) and trace element (ppm) abundance in the sampled websterite xenoliths.

Table 5 Measured Sr and Nd isotopic composition of clinopyroxenes from the sampled xenoliths.

1

	Sample	Type of rock	Ol	Opx	Cpx	Sp	Am	mt+Tmt	Sa	Ga	Pl	T (°C)	T (°C)	P (GPa)
												Wells (1977)	Brey & Köhler (1990)	Harley (1984)
	IG4			20.3	61.6	4.6			3.3	10.2		970	960	1.28
	9Th			17.1	69.8	7.5			1.7	3.9		950	930	1.21
	12Th			34.4	56.5	3.7			3.3	2.1		955	960	
	21Th	Sp-Ga-Sa-bearing websterites		30.7	48.7	11.2			6.3	3.1		925	905	1.3
	IT45			17.9	68.1	1.8		3.2	0.1	8.9		1000	985	1.45
	IT53			8.5	72.5	10.2		0.8	3.1	4.9				
Groupe A	15Th			51.5	44.2	2.3				2		950	940	
	26Th			13.5	72.9	6.4				7.2		955	930	1.34
	IT2	Sp-Ga-bearing websterites		40.5	53.1	2.3				4.1		950	940	1.27
	IT8			41.5	45.8	3.5				9.2		960	955	1.24
	IT28			15.3	60.3	18.5		1.3		4.6		905	895	1.07
	16Th	Sp-bearing websterites		67.7	28.4	3.9						940	940	
	20Th			27.5	63.3	9.2						925	905	
	IT23		6.9	15.4	67.8	4.5		5.4				1050	1080	
	Il10	Sp-Ol-bearing websterites	11.3	16.1	69.4	3.2						905	895	
Groupe B	Il31		2.4	32.3	61.3	4						885		
	IT26	Sp-Am-Ga-Pl-bearing websterite	20.2	72.1	0.5	1.5	0.4		4.2	1.1	1020	1005	1.28	
	IT41	Ga-Am-bearing composite		17.1	32.9		6.5	11.3		9.2	23	815	820	1.15

Table 2

	Group B			Group A												Group B					Group A			
Mineral	**Ol**	**Ol**	**Ol**	**Opx**	**Opx**	**Opx**	**Opx**	**Opx**	**Opx**	**Opx**	**Opx**	**Opx**	**Opx**	**Opx**	**Opx**	**Opx**	**Opx**	**Opx**	**Opx**	**Opx**	**Cpx**	**Cpx**	**Cpx**	**Cpx**
Sample	**IT23**	**II10**	**II31**	**IG4**	**9Th**	**12Th**	**21Th**	**IT45**	**16Th**	**20Th**	**15Th**	**26Th**	**IT2**	**IT8**	**IT28**	**IT23**	**II10**	**II31**	**IT26**	**IT41**	**IG4**	**9Th**	**12Th**	**21Th**
SiO_2	39.75	40.12	42.28	53.05	54.48	52.80	52.49	54.97	54.90	54.31	53.22	54.05	53.98	54.33	53.51	51.78	56.55	55.32	51.85	51.28	51.77	52.21	50.08	50.43
TiO_2	0.08	0.02	0.02			0.08	0.03	0.05	0.07	0.02	0.02	0.09	0.05	0.03	0.12	0.42	0.11	0.05	0.15	0.11	0.10	0.09	0.31	0.12
Al_2O_3	0.06			7.93	5.89	8.17	7.98	5.18	5.57	5.78	7.34	5.82	6.88	5.97	5.70	6.30	2.30	2.81	4.61	4.53	7.19	6.36	8.74	8.65
Cr_2O_3	0.06			0.18	0.14	0.63	0.17	0.16	0.16	0.09	0.12	0.21	0.21	0.24		0.06	0.22	0.21	0.07		0.26	0.22	0.84	0.10
MgO	44.04	54.27	54.54	30.73	31.71	30.57	30.54	32.05	30.84	31.42	30.88	29.83	31.20	31.63	28.76	27.91	31.69	30.82	24.98	24.02	15.79	15.70	14.59	14.61

FeO$_{total}$	16.18	4.87	3.46	7.40	6.67	6.97	7.22	6.78	7.28	7.56	7.49	9.10	7.13	7.16	12.03	11.88	6.85	10	17.26	18.70	2.82	2.57	2.78	3.10
MnO	0.23	0.25	0.27	0.20	0.13	0.17	0.17	0.13	0.19	0.18	0.16	0.17	0.15	0.23	0.18	0.17	0.27	0.26	0.28	0.20	0.09	0.07	0.20	0.10
NiO	0.24	0.27	0.31	0.05	0.07	0.04	0.10	0.10	0.13	0.12	0.09	0.06	0.09	0.08	0.01		0.05	0.06			0.04	0.04	0.03	0.05
CaO	0.11	0.04	0.03	0.69	0.73	0.68	0.81	0.79	0.80	0.52	0.63	0.87	0.57	0.73	0.54	1.29	1.33	0.38	0.63	0.92	22.29	22.21	21.66	22.09
Na_2O			0.03	0.06	0.06	0.07	0.04		0.08	0.10	0.03	0.03		0.05	0.07	0.20	0.73	0.04	0.16	0.09	0.82	0.72	0.85	0.79
K_2O									0.03								0.06						0.04	
Total	100.76	99.84	100.97	100.30	99.88	100.19	99.56	100.21	100.06	100.11	100.00	100.23	100.25	100.44	100.93	100.03	100.15	99.96	99.99	99.88	101.18	100.19	100.13	100.05
mg#	**82.92**	**95.22**	**96.58**	**88.11**	**89.45**	**88.65**	**88.26**	**89.38**	**88.30**	**88.07**	**88.05**	**85.36**	**88.63**	**88.72**	**81.03**	**80.79**	**89.21**	**84.63**	**72.06**	**69.63**	**90.96**	**91.65**	**90.39**	**89.38**

Total Fe as FeOtotal, mg# = 100 x Mg/(Mg+Fe)

	Group A									Group B					Group A									
Mineral	**Cpx**	**Cpx**	**Cpx**	**Cpx**	**Cpx**	**Cpx**	**Cpx**	**Cpx**	**Cpx**	**Cpx**	**Cpx**	**Cpx**	**Cpx**	**Cpx**	**Sp**	**Sp**	**Sp**	**Sp**	**Sp**	**Sp**	**Sp**	**Sp**	**Sp**	**Sp**
Sample	**IT45**	**IT53**	**16Th**	**20Th**	**15Th**	**26Th**	**IT2**	**IT8**	**IT28**	**IT23**	**Il10**	**Il31**	**IT26**	**IT41**	**IG4**	**9Th**	**12Th**	**21Th**	**IT45**	**IT53**	**16Th**	**20Th**	**15Th**	**26Th**
SiO_2	52.23	51.07	51.64	51.87	50.94	50.88	50.55	51.26	50.46	48.81	53.52	52.21	48.71	48.47	0.05		0.06	0.02	0.07	0.02	0.02	0.07	0.05	0.05
TiO_2	0.08	0.07	0.38	0.15	0.24	0.18	0.34	0.10	0.92	1.32	0.52	0.49	1.38	1.39	0.29			0.02	0.02	0.06			0.06	0.03
Al_2O_3	6.58	8.50	6.47	6.20	8.25	6.54	8.26	7.05	7.85	8.69	4.12	4.21	8.54	8.73	66.84	67.22	59.11	68.57	65.15	68.47	64.03	64.28	64.05	62.74
Cr_2O_3	0.23	0.12	0.39	0.26	0.36	0.25	0.33	0.38	0.03	0.06	0.75	0.78	0.06		2.04	2.87	8.86	1.68	2.50	1.17	3.63	2.35	1.52	2.40
MgO	15.40	14.32	15.39	15.27	14.62	15.59	14.99	15.44	13.51	14.33	15.09	15.13	11.51	11.06	22.47	22.41	21.26	20.68	20.43	21.29	20.76	21.09	21.13	19.53
FeO_{total}	3.16	2.51	3.00	2.97	3.03	4.41	2.85	3.04	4.92	6.74	3.75	3.71	8.04	8.16	8.06	6.86	9.41	7.79	10.67	8.46	10.66	10.60	10.93	13.90
MnO	0.07	0.06	0.06	0.12	0.09	0.08	0.06	0.13	0.10	0.18	0.12	0.15	0.11	0.11	0.10	0.06	0.13	0.11	0.14	0.09	0.10	0.11	0.19	0.20
NiO	0.05	0.02	0.05	0.05	0.04		0.04	0.04	0.03	0.05	0.01	0.03			0.14	0.33	0.23	0.36	0.47	0.34	0.57	0.50	0.41	0.28

CaO	21.52	23.00	21.52	21.80	21.62	21.44	22.16	21.82	21.10	18.66	22.52	22.49	20.26	20.14								0.02	0.03	0.02			
Na_2O	0.78	0.66	1.07	0.95	0.99	0.62	0.67	0.74	1.14	1.31	0.76	0.77	1.77	1.86								0.03	0.03	0.02			
K_2O	0.03	0.02								0.04						0.02	0.02	0.03				0.02	0.01		0.04		
Total	100.13	100.36	99.97	99.64	100.17	100.00	100.25	100.00	100.04	100.22	101.17	99.96	100.38	99.94	99.98	99.78	99.09	99.27	99.45	99.89	99.84	99.09	98.38	99.17			
mg#	**89.63**	**91.03**	**90.15**	**90.20**	**89.56**	**86.34**	**90.39**	**89.99**	**83.06**	**79.20**	**87.76**	**87.95**	**72.01**	**70.78**	**83.23**	**85.33**	**82.07**	**82.54**	**77.78**	**81.77**	**79.45**	**80.71**	**81.07**	**75.43**			
cr#	**-**	**-**	**-**	**-**	**-**	**-**	**-**	**-**	**-**	**-**	**-**	**-**	**-**	**-**	**2.01**	**2.78**	**9.13**	**1.62**	**2.51**	**1.14**	**3.64**	**2.39**	**1.59**	**2.52**			

Total Fe as FeOtotal, mg#= 100 x Mg/(Mg+Fe), cr#= 100 x Cr/(Cr+Al)

	Group A			Group B			Group B	Group A							Group B			Group A						Group B	
Mineral	Sp	Sp	Sp	Sp	Sp	Sp	Pl	Ga	Ga	Ga	Ga	Ga	Ga	Ga	Ga	Ga	Ga	Sa	Sa	Sa	Sa	Sa	Sa	Amp	Amp
Sample	IT2	IT8	IT28	IT23	II31	IT26	IT26	IG4	9Th	IT45	IT53	26Th	IT2	IT8	IT28	IT26	IT41	IG4	9Th	12Th	21Th	IT45	IT53	IT26	IT41
SiO_2	0.04	0.03	0.05	0.06	0.03	0.03	57.10	42.30	43.02	41.81	42.34	41.50	41.41	42.63	41.00	40.62	40.05	15.30	15.07	14.77	15.63	15.53	14.79	43.22	40.72
TiO_2	0.03	0.01	0.10	0.70	0.16	0.45		0.05		0.02		0.05	0.10	0.04	0.09	0.11	0.13	0.03	0.08	0.06	0.05	0.02	0.02	1.58	4.36
Al_2O_3	63.1	63.13	64.18	47.06	49.63	52.49	27.47	23.96	23.09	24.09	24.02	23.42	24.46	23.65	23.36	22.34	22.28	58.94	59.64	56.51	58.03	59.97	61.02	15.00	13.82
Cr_2O_3	4.42	4.81	0.01	1.04	16.08	3.24		0.24	0.27	0.18	0.15	0.16	0.42	0.34		0.02	0.01	1.43	1.43	4.34	0.69	1.19	0.51	0.61	
MgO	21.16	21.05	17.76	17.80	19.92	11.82		19.82	21.56	18.56	18.66	17.99	18.92	19.69	15.45	13.09	11.63	19.71	19.98	19.45	19.89	19.68	19.70	16.20	11.92
FeO$_{total}$	10.04	10.51	17.20	32.34	12.09	30.46	0.13	7.69	4.35	8.83	8.05	10.56	8.51	8.72	14.30	19.22	20.09	4.25	3.49	3.78	4.11	4.11	3.92	6.63	12.58
MnO	0.09	0.08	0.12	0.20	0.16	0.34		0.32	0.20	0.42	0.43	0.47	0.25	0.44	0.57	0.98	0.60	0.04	0.05	0.10	0.05	0.09			0.03
NiO	0.46	0.29	0.18	0.42	0.30	0.11			0.06						0.03			0.17	0.13	0.12	0.12	0.17	0.15	0.08	
CaO							8.69	5.91	6.41	5.37	7.14	5.94	6.15	5.77	5.88	4.74	5.85	0.06	0.06	0.09	0.09	0.07	0.06	11.70	10.82
Na_2O							6.59	0.16	0.53	0.65	0.24				0.10	0.33			0.05					3.50	2.81
K_2O							0.16		0.13	0.06														0.28	1.30
Total	99.39	99.93	99.62	99.65	98.40	98.95	10 0.20	10 0.47	99.62	10 0.00	10 1.02	10 0.09	10 0.24	10 1.30	10 0.81	10 1.45	10 0.66	99.94	99.97	99.24	99.27	10 0.84	10 0.21	98.81	98.36
mg#	**80.95**	**79.86**	**68.17**	**71.70**	**80.36**	**48.85**	**16.67**	**84.24**	**95.78**	**83.77**	**83.30**	**77.12**	**81.37**	**81.50**	**68.13**	**58.21**	**52.08**	**91.72**	**93.76**	**92.76**	**91.58**	**90.61**	**92.74**	**90.02**	**66.45**
cr#	**4.46**	**4.86**	**0.00**	**1.45**	**17.86**	**3.98**	-	-	-	-	-	-	-	-	-	-	-	-	-	-	-	-	-	-	-

Total Fe as FeOtotal, mg#= 100 x Mg/(Mg+Fe), cr#= 100 x Cr/(Cr+Al)

3

	Group A									Group B		
Site	**IG**	**IT**	**IT**	**IT**	**IT**	**IT**	**IT**	**IT**	**IT**	**II**	**IT**	**IT**
Sample	**IG4**	**9Th**	**12Th**	**IT45**	**IT53**	**16Th**	**15Th**	**IT2**	**IT8**	**II31**	**IT26**	**IT41**
Sc	49.1	52.6	74.5	33.5	20.1	55.9	57.2	27.8	28.3	53.9	77.4	72.6
Ti	769	861	1943	572	272	1814	1328	1655	603	2819	8417	8339
V	314	203	213	504	174	230	307	272	327	232	286	290
Ni	385	238	191	370	261	441	323	393	267	255	53.3	78
Rb		0.40										
Sr	0.75	10.4	21.9	24.8	1.41	15.6	18	3.29	4.5	24	69	132
Y	7.93	4.43	11.9	5.87	0.96	15.9	15.6	3.19	3.47	11.1	34.9	32.3
Zr	1.61	5.03	7.78		2.78	9.20	6.24	12.2	3.16	14.3	161	146
Nb	0.03		0.33	0.97	0.04	0.45	0.30			0.21	0.41	0.55
Ba	0.03	0.10	0.11	2.14	2.42	0.10	0.06	0.21	0.04	0.26	0.13	1.40
La		0.27	0.20	1.04		0.44	1.52	0.04		0.70	6.42	6.04
Ce	0.15	0.85	0.95	2.59	0.02	0.87	3.14	0.23	0.21	2.81	27.7	24.5
Pr		0.20	0.28	0.35	0.02	0.13	0.42	0.09	0.07	0.57	5.85	4.62
Nd	0.40	1.14	2.59	1.40	0.25	1.20	1.98	0.99	0.68	3.51	32.6	24.6
Sm	0.31	0.45	1.16	0.35	0.12	0.71	0.70	0.59	0.42	1.39	9.05	7.16
Eu	0.19		0.29	0.12	0.06	0.41	0.32	0.24	0.17	0.55	3.04	2.34
Gd	0.93	0.69	1.69	0.54	0.23	1.61	1.38	0.78	0.90	1.96	9.24	7.41
Tb	0.19	0.14	0.31	0.12	0.04	0.27	0.29	0.13	0.15	0.35	1.35	1.11
Dy	1.49	0.87	1.91	0.87	0.20	2.66	2.47	0.75	0.84	2.15	7.85	6.64
Ho	0.33	0.21	0.46	0.19	0.04	0.63	0.62	0.14	0.15	0.41	1.43	1.25
Er	0.95	0.51	1.39	0.57	0.09	1.70	1.90	0.36	0.40	1.07	3.51	3.14
Yb	0.81	0.50	1.25	0.56	0.08	1.73	1.90	0.31	0.34	0.89	2.95	2.73
Lu	0.10	0.07	0.17	0.09		0.26	0.28	0.04	0.04	0.12	0.38	0.35
Hf		0.35	0.50			0.55						
Pb				0.09			0.36			0.13	0.16	0.25
Th			0.27	0.10		0.07	0.28		0.05	0.05	0.03	0.08
U			0.05	0.02			0.12			0.04		0.03
$[La/Sm]_N$		**0.38**	**0.11**	**1.89**		**0.39**	**1.35**	**0.04**		**0.31**	**0.44**	**0.53**
$[La/Yb]_N$		**0.34**	**0.10**	**1.16**		**0.16**	**0.50**	**0.07**		**0.49**	**1.36**	**1.39**
$[Sm/Yb]_N$	**0.24**	**0.56**	**0.58**	**0.39**	**0.99**	**0.26**	**0.23**	**1.22**	**0.79**	**0.98**	**1.92**	**1.65**

4

	Group A													Group B				
Site	**IG**	**IT**	**IT**	**IT**	**IT**	**IT**	**IT**	**IT**	**IT**	**IT**	**IT**	**IT**	**IT**	**IT**	**II**	**II**	**IT**	**IT**
Sample	**IG4**	**9Th**	**12Th**	**21Th**	**IT45**	**IT53**	**15Th**	**26Th**	**IT2**	**IT8**	**16Th**	**20Th**	**IT28**	**IT23**	**II10**	**II31**	**IT26**	**IT41**
SiO$_2$	46.93	45.13	47.12	47.01	48.80	44.24	49.16	46.35	48.24	47.25	49.57	45.66	41.59	43.06	49.18	48.80	41.74	39.81
TiO$_2$	0.12	0.12	0.17	0.11	0.06	0.05	0.13	0.13	0.13		0.14	0.11	0.52					
Al$_2$O$_3$	12.86	13.96	10.80	12.88	9.72	15.88	8.67	10.33	10.93	11.77	7.87	11.41	16.26	12.47	4.68	4.37	12.24	11.77
Fe$_2$O$_{3total}$	4.88	3.68	5.39	5.95	5.22	4.28	5.81	6.42	5.86	6.27	6.73	5.23	10.41	10.82	8.16	7.83	18.05	17.78
Mn O	0.13	0.09	0.16	0.13	0.15	0.10	0.14	0.17	0.13	0.18	0.13	0.12	0.17	0.15	0.15	0.15	0.29	0.19
Mg O	18.69	16.51	22.00	22.33	18.28	15.32	23.51	17.43	21.69	21.45	26.50	19.87	16.98	18.54	21.57	20.96	14.10	11.52
Ca O	14.82	18.29	10.35	11.46	15.62	18.85	9.93	16.57	12.13	11.33	6.60	13.59	12.93	12.63	14.29	14.18	9.88	10.84
Na$_2$O	1.47	0.00	0.00	0.58	0.00	0.57	0.00	0.10	0.38	0.78	0.00	0.00	0.58	1.09	0.56	0.00	1.83	0.85
K$_2$O	0.00	0.00	0.00	0.00	0.00	0.00	0.00	0.00	0.00	0.03	0.00	0.00	0.00	0.03	0.08	0.05	0.10	0.16
P$_2$O$_5$	0.02	0.03	0.03	0.03	0.07	0.00	0.03	0.04	0.00	0.00	0.05	0.04	0.00	0.01	0.00	0.05	0.07	0.10
LOI	0.46	0.29	0.37	0.50	0.24	0.42	0.35	0.31	0.50	0.41	0.40	0.40	0.29	0.12	0.32	0.31	0.67	1.00
Total	100.10	98.09	96.38	101.04	98.17	99.72	97.73	97.84	100.05	99.56	97.99	96.46	99.73	99.96	99.33	97.03	100.37	96.59
mg#	**88.36**	**89.89**	**88.99**	**88.13**	**87.40**	**87.63**	**88.90**	**84.32**	**88.00**	**87.13**	**88.63**	**88.28**	**76.88**	**77.24**	**83.97**	**84.13**	**60.75**	**56.21**
Sc		22.53	17.70	11.83	25.07	19.00	16.10	28.31	19.38	21.20	12.74	14.74	20.61	17.36	20.89	20.61	16.81	16.59
Ti		8.76	519.52	3.81	0.78	8.57	7.80	1.80	7.38	212.73	6.69	1.98	1356.64	297.11	100.09	997.64	351.61	710.16
V		0.65	93.56	68.35	4.23	82.71	2.46	3.77	1.81	121.88	65.64	69.38	2.43	161.46	96.86	94.40	122.75	181.31
Cr		3.72	7.35	8.15	0.93	4.20	0.74	1.03	0.36	112.07	0.74	5.08	10.71	243.38	209.23	200.98	420.02	51.32
Co		16.63	19.51	19.88	18.54	14.98	24.35	16.97	21.04	19.37	24.71	18.38	21.38	27.41	29.67	28.36	27.98	33.32
Ni		3.58	179.90	0.07	0.68	0.59	9.09	9.27	4.10	171.59	3.98	8.33	8.27	192.88	278.91	270.15	74.75	120.25
Cu		2.55	2.45	3.92	1.91	11.48	2.69	1.86	1.46	1.96	7.43	4.95	33.39	4.45	6.80	7.03	13.72	14.69
Zn		10.03	10.64	8.68	13.91	9.10	14.38	13.33	89.52	108.61	14.41	13.51	18.68	22.21	65.58	23.76	71.78	38.59
Ga		2.55	2.27	2.03	2.86	2.28	2.72	2.81	2.87	2.15	1.92	2.20	4.38	5.16	2.33	2.25	8.86	8.51
Rb		0.10	0.07	0.12	0.31	0.00	0.00	0.00	0.20	0.07	0.02	0.03	0.01	0.09	0.47	0.47	0.22	0.59
Sr		5.39	7.90	6.32	4.05	1.81	6.51	9.98	9.33	4.67	4.77	4.11	15.14	28.49	9.79	9.31	74.21	150.65
Y		2.26	2.68	2.11	4.11	1.55	4.09	3.41	3.83	3.92	2.58	2.65	6.31	5.24	3.29	3.05	9.62	7.36
Zr		2.09	2.49	1.51	1.55	5.02	9.21	1.90	0.82	2.24	2.21	1.97	6.90	13.79	3.88	3.93	28.58	29.89
Nb		0.07	0.29	0.16	0.37	0.07	0.84	0.47	0.40	0.31	0.35	0.27	0.20	0.28	0.12	0.13	0.28	1.51

Ba	2.83	8.49	14.96	4.02	2.81	5.04	5.01	93.29	21.29	2.61	5.66	17.83	9.75	2.07	2.16	119.41	44.70
La	0.25	0.24	0.11	0.24	0.03	0.54	0.18	0.21	0.07	0.22	0.36	0.31	0.63	0.22	0.25	1.97	2.36
Ce	0.53	0.55	0.23	0.46	0.04	0.87	0.25	0.40	0.14	0.38	0.42	0.90	2.19	0.81	0.87	5.65	6.63
Pr	0.09	0.10	0.03	0.05	0.01	0.11	0.05	0.06	0.03	0.06	0.08	0.19	0.40	0.16	0.17	1.14	1.13
Nd	0.48	0.46	0.20	0.32	0.05	0.74	0.33	0.30	0.21	0.31	0.39	1.26	2.43	1.02	1.03	6.39	5.89
Sm	0.17	0.16	0.11	0.07	0.04	0.07	0.12	0.04	0.13	0.04	0.05	0.28	0.90	0.40	0.39	1.90	1.64
Eu	0.07	0.05	0.05	0.03	0.03	0.07	0.06	0.06	0.06	0.06	0.08	0.24	0.36	0.16	0.15	0.68	0.63
Gd	0.26	0.27	0.14	0.02	0.02	0.04	0.22	0.09	0.29	0.07	0.08	0.22	1.13	0.56	0.54	2.00	1.67
Tb	0.05	0.07	0.05	0.06	0.03	0.08	0.08	0.07	0.07	0.06	0.06	0.17	0.19	0.10	0.10	0.32	0.26
Dy	0.37	0.44	0.33	0.55	0.22	0.66	0.66	0.55	0.58	0.43	0.46	1.18	1.16	0.66	0.62	1.97	1.57
Ho	0.07	0.10	0.07	0.15	0.05	0.16	0.14	0.14	0.15	0.11	0.12	0.31	0.22	0.13	0.13	0.40	0.30
Er	0.25	0.33	0.25	0.55	0.19	0.55	0.44	0.44	0.48	0.33	0.33	0.77	0.59	0.38	0.36	1.09	0.82
Tm	0.04	0.05	0.04	0.09	0.03	0.08	0.06	0.07	0.07	0.05	0.05	0.10	0.07	0.05	0.05	0.15	0.11
Yb	0.23	0.35	0.24	0.26	0.17	0.45	0.36	0.39	0.51	0.33	0.29	0.66	0.42	0.33	0.31	0.93	0.66
Lu	0.03	0.06	0.04	0.01	0.03	0.08	0.05	0.08	0.08	0.05	0.04	0.09	0.06	0.05	0.04	0.14	0.09
Hf	0.07	0.10	0.07	0.03	0.01	0.08	0.04	0.08	0.05	0.01	0.06	0.01	0.55	0.16	0.17	1.06	0.96
Ta	0.01	0.03	0.02	0.02	0.03	0.02	0.02	0.04	0.02	0.02	0.05	0.02	0.03	0.01	0.01	0.05	0.09
Pb	0.05	0.00	0.06	0.07	0.03	0.00	0.08	0.01	0.29	0.02	0.06	0.00	0.10	0.00	0.16	0.00	0.14
Th	0.01	0.05	0.01	0.03	0.00	0.09	0.01	0.02	0.00	0.02	0.02	0.01	0.02	0.01	0.02	0.01	0.03
U	0.00	0.02	0.01	0.01	0.01	0.04	0.00	0.01	0.00	0.01	0.01	0.01	0.01	0.01	0.01	0.01	0.02
$[La/Sm]_N$	**0.92**	**0.59**	**0.61**	**2.07**	**0.48**	**2.01**	**0.53**	**0.97**	**0.37**	**1.00**	**1.46**	**0.33**	**0.44**	**0.35**	**0.39**	**0.65**	**0.90**
$[La/Yb]_N$	**0.68**	**0.43**	**0.29**	**0.25**	**0.13**	**0.62**	**0.31**	**0.28**	**0.09**	**0.42**	**0.77**	**0.29**	**0.93**	**0.43**	**0.50**	**1.33**	**2.24**
$[Sm/Yb]_N$	**0.46**	**0.40**	**0.30**	**0.07**	**0.15**	**0.19**	**0.37**	**0.18**	**0.15**	**0.26**	**0.35**	**0.55**	**1.32**	**0.77**	**0.80**	**1.28**	**1.56**

5

Sample	Type of rock	Sm (ppm)	Nd (ppm)	$^{87}Sr/^{86}Sr$	$^{143}Nd/^{144}Nd$	$^{147}Sm/^{144}Nd$	ε_{Nd}	Model Age TDM (Ma)
IG4		0.311	0.399	0.704453	0.514024	0.469	27.08	515
12Th	**Sp-Ga-Sa-bearing websterites**	1.162	2.587	0.702970	0.512953	0.270	6.14	-567
IT53		0.123	0.25	0.706177	0.513296	0.296	12.84	247
IT2	**Sp-Ga-bearing websterites**	0.592	0.99	0.703790	0.513850	0.360	23.64	717
IT8		0.420	0.68	0.703436	0.513306	0.372	13.03	138

Highlights

- Spinel-garnet-sapphirine-websterite xenoliths have a tholeiitic affinity.
- Spinel-olivine-plagioclase-websterites have an alkaline affinity.
- Composition of clinopyroxenes is consistent with metasomatism by silicate melts.
- Websterite xenoliths originated from the shallow lithospheric mantle.
- Websterite xenoliths highlight crustal growth of the eastern Mediterranean Province.

Declaration of interest statement

The authors Mohamed Ismail, Guillaume Delpech, Bertrand Moine, Michel Grégoire, Colette Guilbaud and Jean Yves Cottin declare that there is no conflict of interest for this study

We the undersigned declare that this manuscript is original, has not been published before and is not currently being considered for publication elsewhere.

We confirm that the manuscript has been read and approved by all named authors and that there are no other persons who satisfied the criteria for authorship but are not listed. We further confirm that the order of authors listed in the manuscript has been approved by all of us.

We understand that the Corresponding Author is the sole contact for the Editorial process. He/she is responsible for communicating with the other authors about progress, submissions of revisions and final approval of proofs.

Signed by the corresponding author:

Jean Yves Cottin

Figure

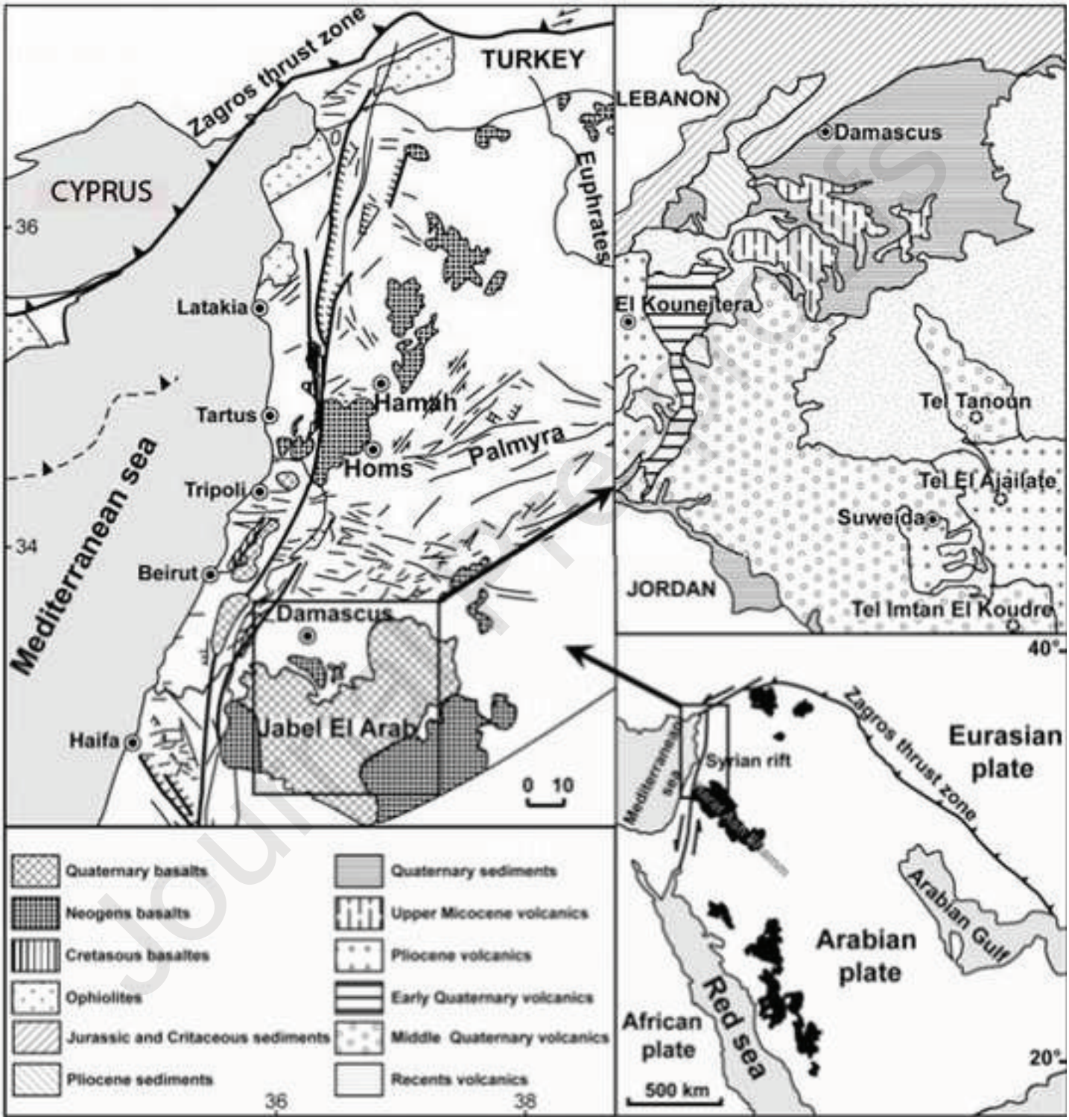
Zagros thrust zone
TURKEY
CYPRUS
LEBANON
Damascus
Euphrates
36
Latakia
El Kounejtera
Hamah
Tartus
Palmyra
Tel Tanoun
Homs
Mediterranean sea
Tripoli
Tel El Ajaiate
Suweida
34
Beirut
JORDAN
Damascus
Tel Imtan El Koudre
40°
Jabel El Arab
Haifa
0 10
Eurasian plate
Syrian rift
Mediterranean sea
Zagros thrust zone
Arabian Gulf
Arabian plate
Red sea
African plate
20°
500 km
Quaternary basalts
Neogens basalts
Cretasous basaltes
Ophiolites
Jurassic and Critaceous sediments
Pliocene sediments
Quaternary sediments
Upper Micocene volcanics
Pliocene volcanics
Early Quaternary volcanics
Middle Quaternary volcanics
Recents volcanics
36
38

Figure

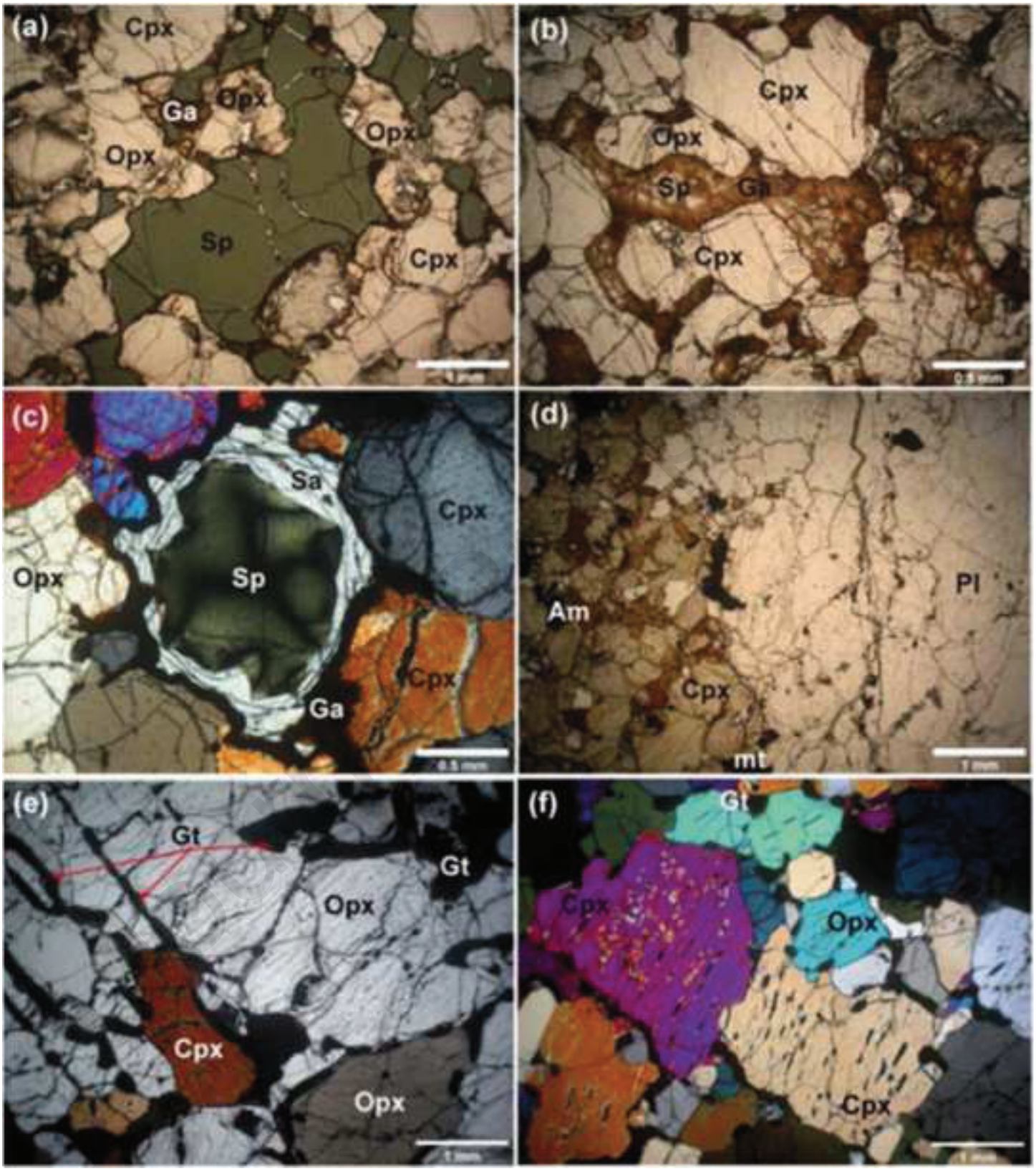
(a)
Cpx
Ga
Opx
Opx
Opx
Sp
Cpx
(b)
Cpx
Opx
Sp
Ga
Cpx
(c)
Sa
Cpx
Opx
Sp
Cpx
Ga
(d)
Pl
Am
Cpx
mt
(e)
Gt
Gt
Opx
Cpx
Opx
(f)
Gt
Cpx
Opx
Cpx

Figure

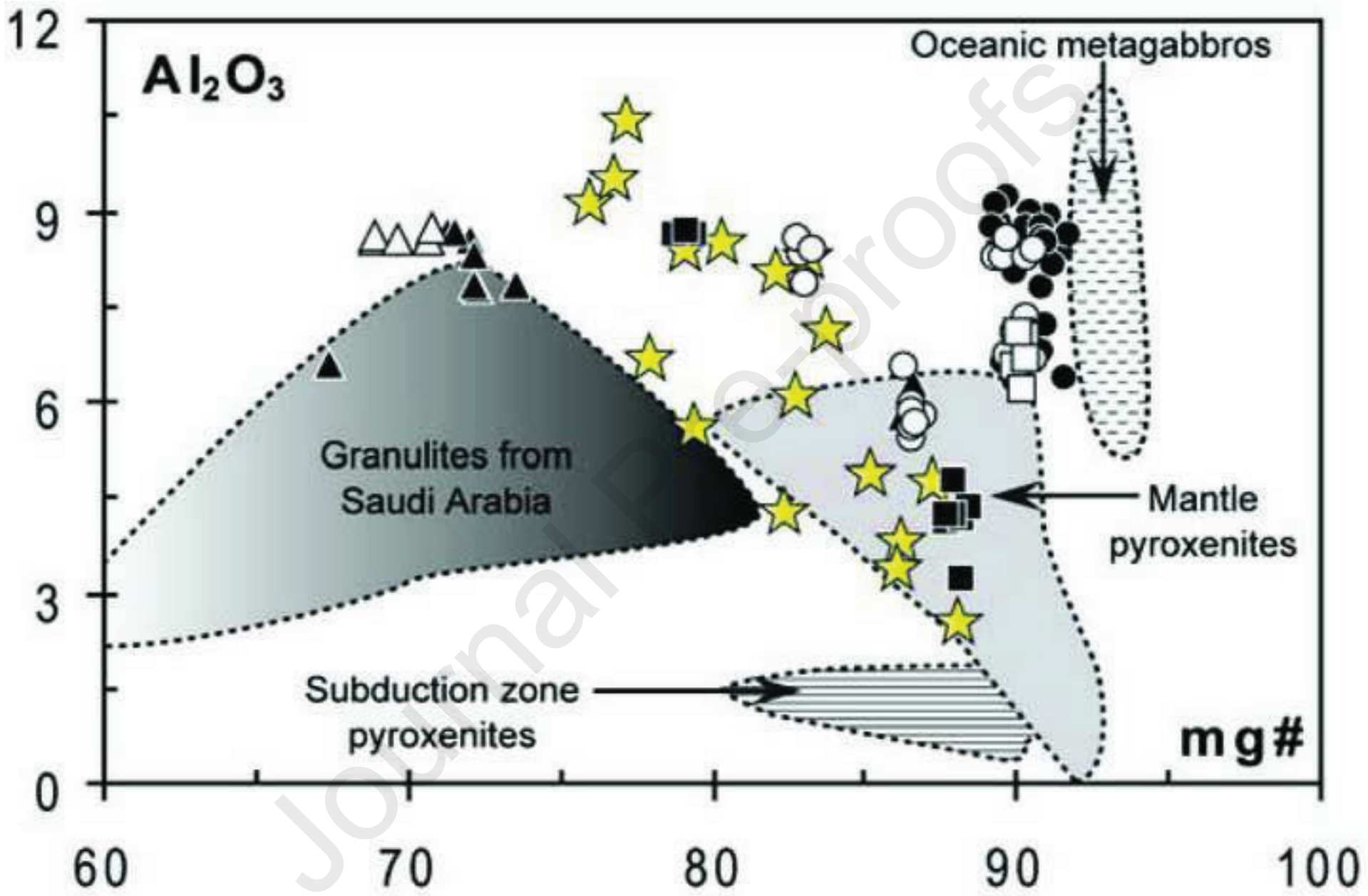

Figure

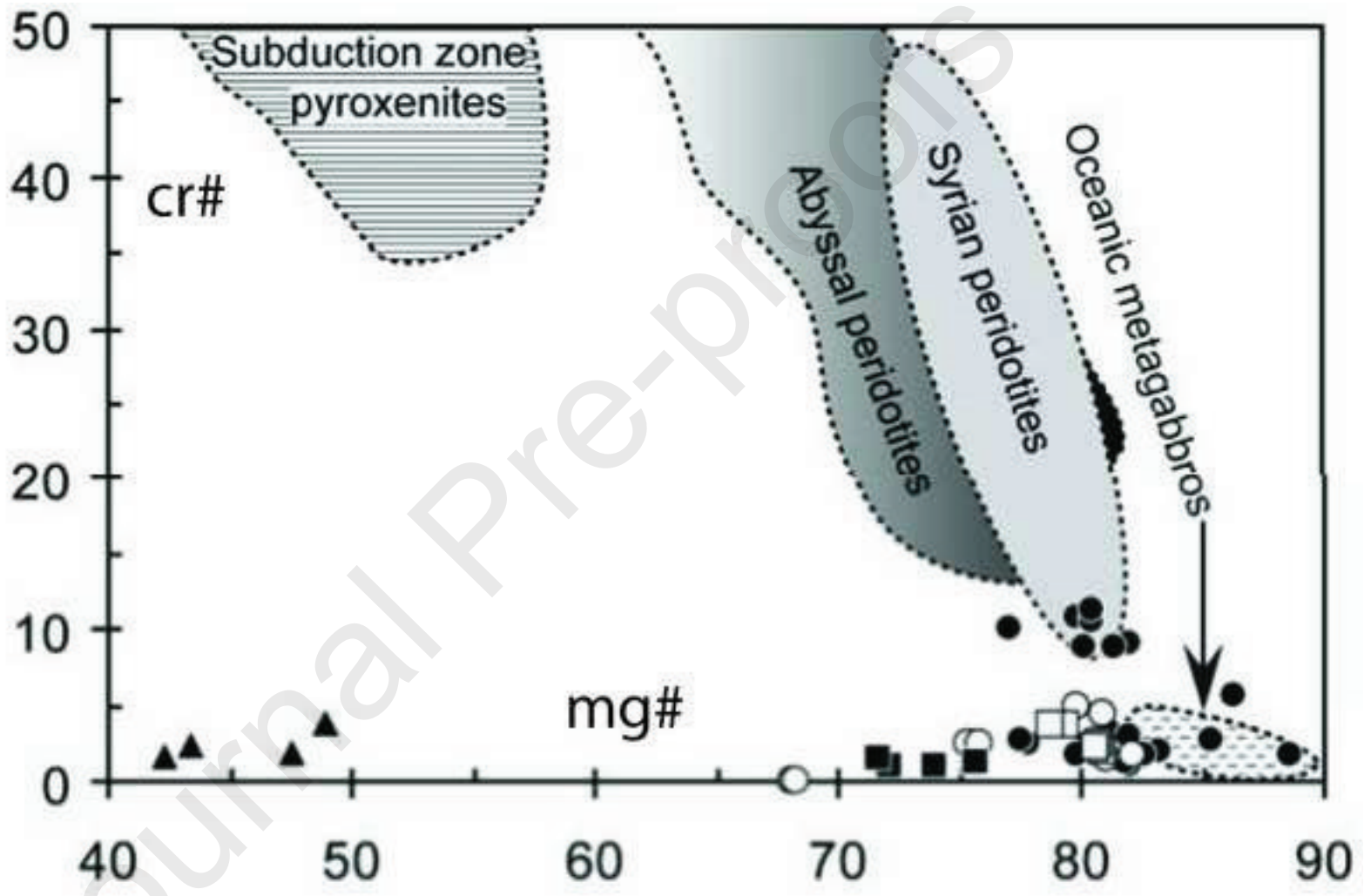

Figure

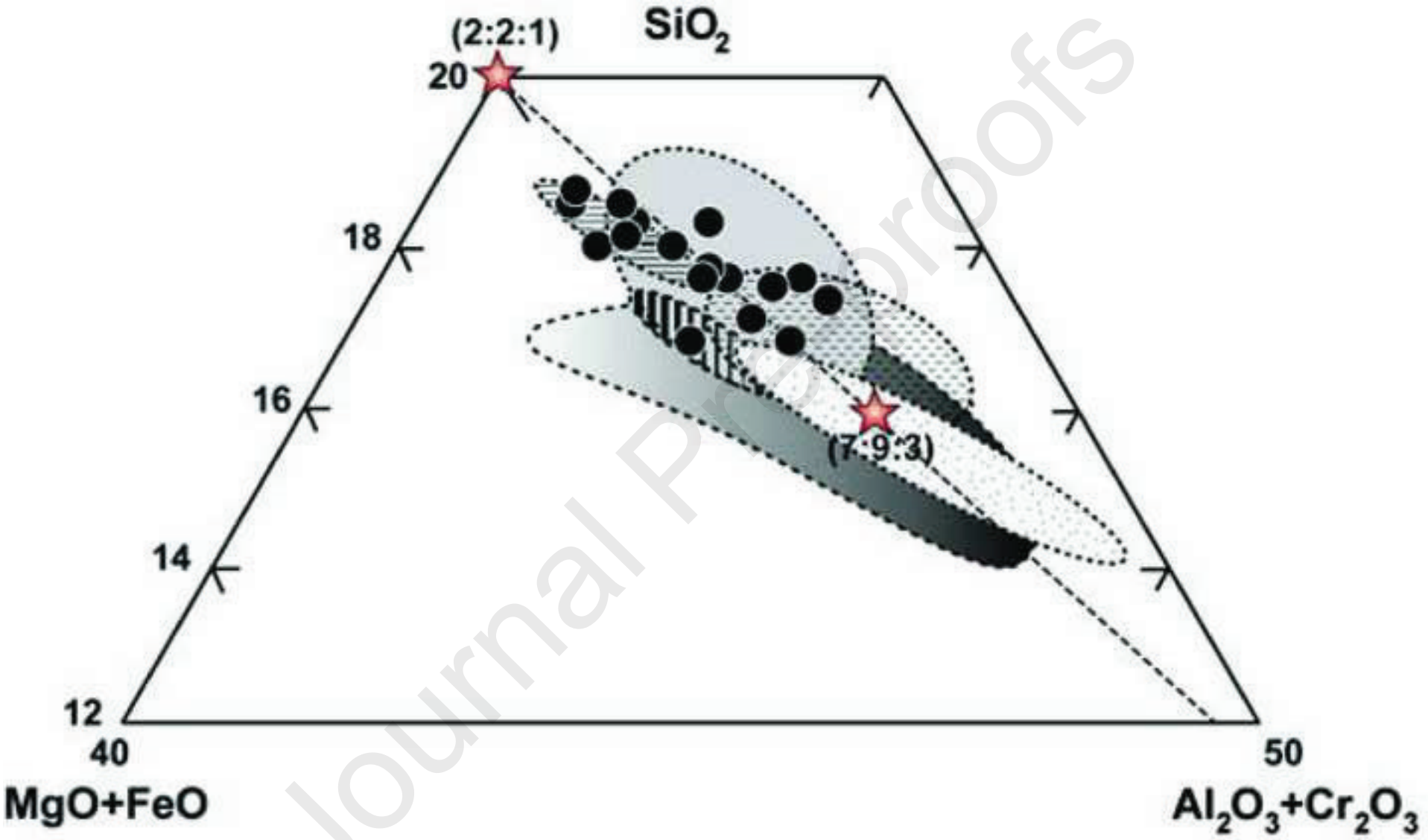

Figure

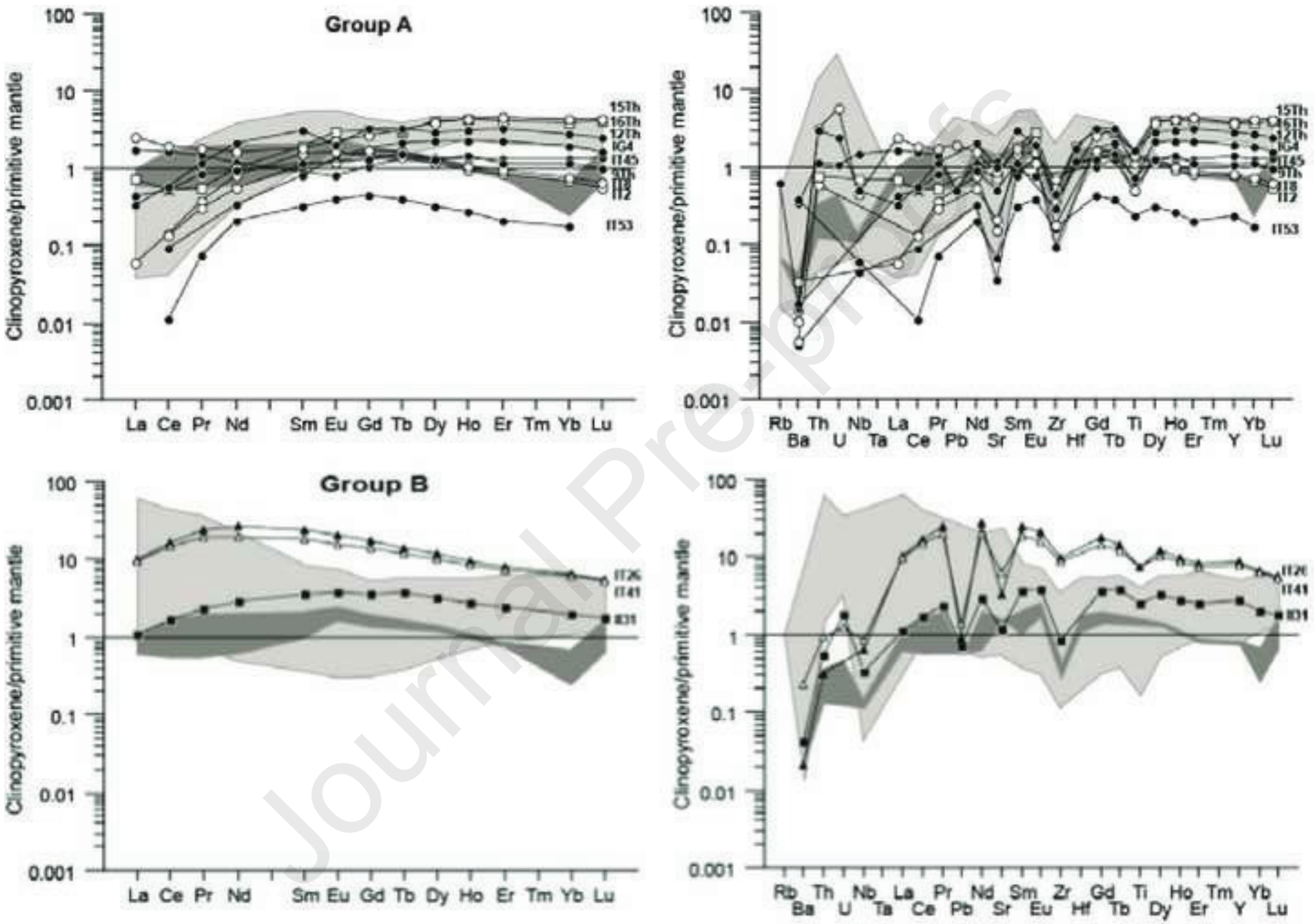

Figure

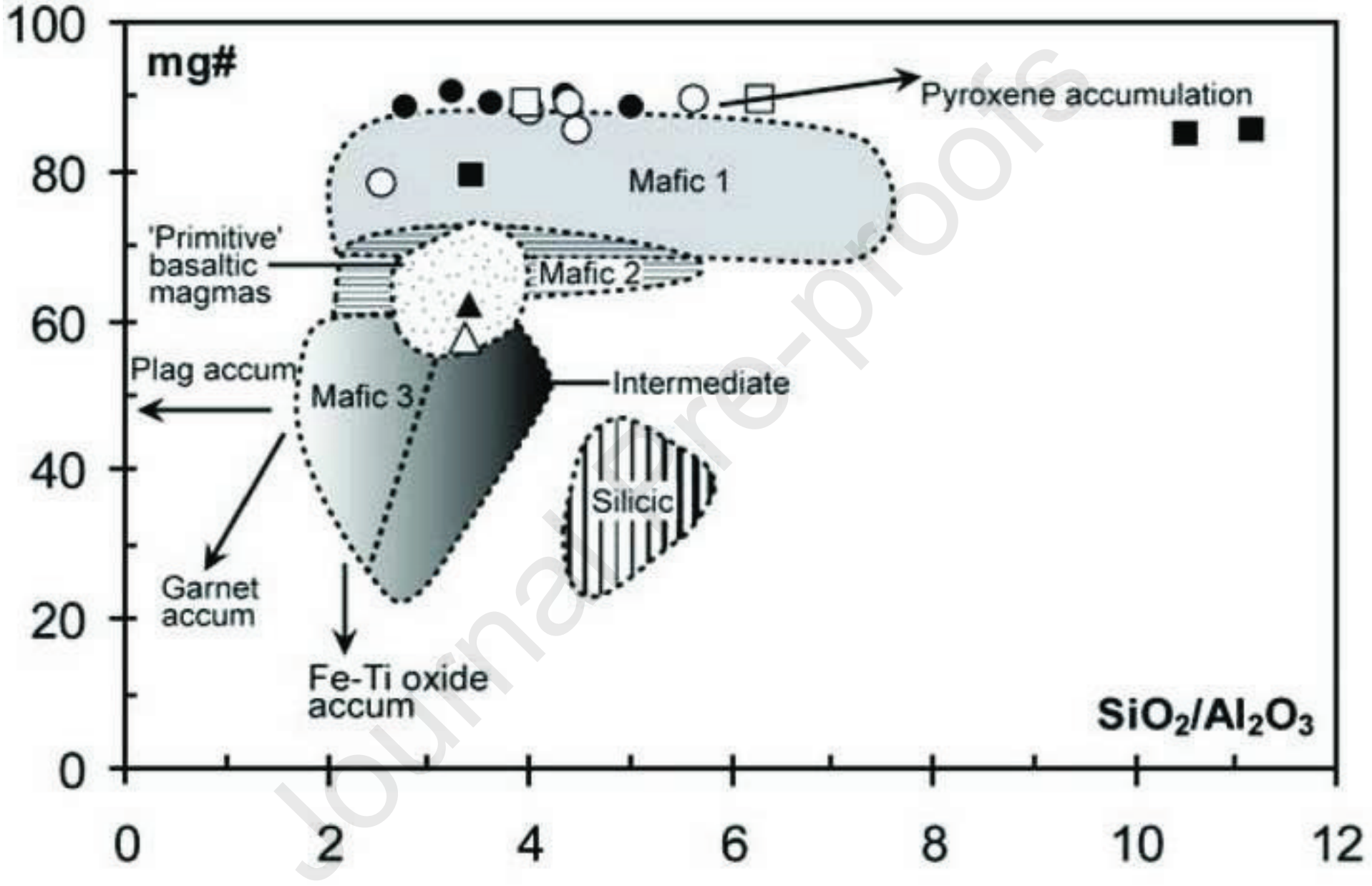

Figure

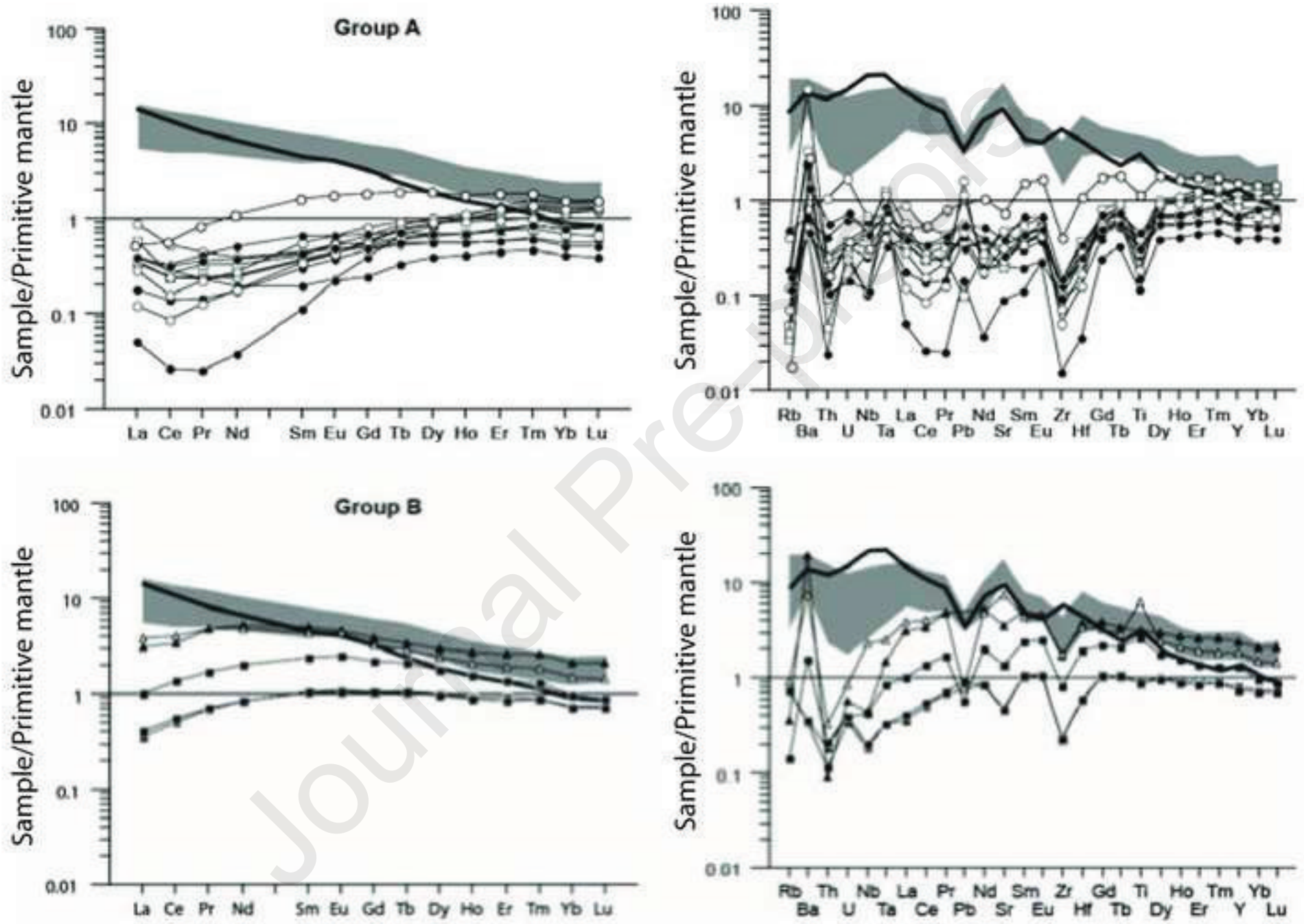

Figure

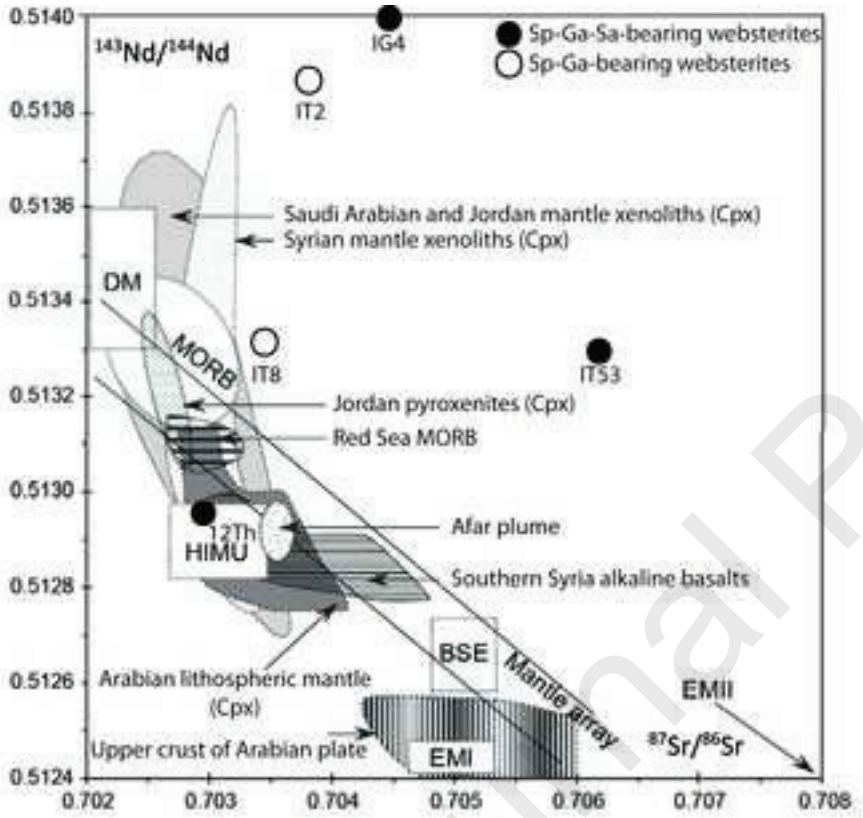

Figure